NOVEL POLARIMETERY TECHNIQUES

A Dissertation
Presented to
The Academic Faculty

by

Neeraj Kothari

In Partial Fulfillment
of the Requirements for the Degree
Doctor of Philosophy in the
School of Physics

Georgia Institute of Technology
December 2007

NOVEL POLARIMETRY TECHNIQUES

Approved by:

Dr. Rick Trebino, Advisor
School of Physics
Georgia Institute of Technology

Dr. Ahmet Erbil
School of Physics
Georgia Institute of Technology

Dr. Andreas S. Bommarius
School of Chemical & Biomolecular Engineering
Georgia Institute of Technology

Dr. Chandra Raman
School of Physics
Georgia Institute of Technology

Dr. Philip N. First
School of Physics
Georgia Institute of Technology

Date Approved: July 20, 2007

To my dear grandparents, loving parents and beloved wife

ACKNOWLEDGEMENTS

I am very grateful to my advisor Prof. Rick Trebino for all the opportunities and support, both scientific and otherwise, that made this dissertation possible. I am also grateful to Prof. Andreas S. Bommarius, who as co-advisor had advised me on the chemical and biological materials, and challenges I could overcome while doing my research.

I appreciate and thank all the post-doctoral students Dr. Erik Zeek, Dr. Xun Gu, Dr. Selcuk Aturk and especially Dr. Aliakbar Jafarpour for helping me with the theory and experiments. I am very thankful to Mark Kimmel, lab manager with the Trebino group during my initial years to help me pick up and hone my experimental skills. I also thank Dr. Aparna, Pablo, Dongjoo, Xuan, Pamela and Lina who have been wonderful labmates, for all the great times of learning and otherwise, in and outside the lab.

I especially thank Edwin and Elizabeth Greco, whom I met after enrolling in the PhD program, for becoming my family away from home.

Finally, I am extremely grateful to my parents, and my beloved wife for their endless love, encouragement and sacrifices.

I would like to acknowledge NASA (Astrobiology Science and Technology for Instrument Development, grant number NNG04GM70G) for financial support. I also thank Robert Tillman and Vladimir Kupershmidt of the former Sunshine Medical Corp., for helpful discussions.

TABLE OF CONTENTS

LIST OF TABLES

LIST OF FIGURES

LIST OF SYMBOLS AND ABBREVIATIONS

Symbol or Abbreviation	Meaning
3H	Third Harmonic
4H	Fourth Harmonic
BBO	beta - Barium Borate
DFG	Difference Frequency Generation
DLS	Depolarizing Light Scattering
E	Extraordinary polarization
ER	Extinction Ratio
HWP	Half-Wave Plate
IR	Infra-Red
NLFE	Nonlinear Faraday Effect
NLO	Non-Linear Optical
O	Ordinary polarization
OPA	Optical Parametric Amplification
OPO	Optical Parametric Oscillation
OR	Optical Rectification
QWP	Quarter-Wave Plate
RP	Rotating Polarization
SFG	Sum Frequency Generation
SH	Second Harmonic
SHG	Second Harmonic Generation
TGG	Terbium Gallium Garnet
UV	Ultra-Violet

SUMMARY

Polarization specific measurements are advancing the capabilities of scientific instruments looking for ever smaller effects and material parameters. For example, the magneto-optical nonlinear Faraday effect can be used to characterize various electric and magnetic polarizability parameters of an individual molecule. Another major application is detection of desired particles in a highly scattering environment, the physical effect of which has been extensively researched, and is being overcome by using time-gated and polarization techniques. The polarimeter sensitivity is limited by the extinction-ratio obtained from polarizers. Of available polarizer materials, naturally occurring Calcite crystals provide the best extinction ratios because of their good optical homogeneity and high birefringence. However, there is a need for polarization determination with higher sensitivities, and thus a necessity to find better polarizing materials and methods.

I developed a next-generation polarimeter in an attempt to sensitively detect the second-order Faraday effect, along with a substance's chirality and Verdet constant. Also, I developed a device uniquely able to sensitively detect chiral signatures in the presence of massive depolarizing scattering. In addition, I begun developing a novel type of polarimeter based on the highly-polarization-sensitive nonlinear-optical process of harmonic generation, whose required crystals can be grown with extremely high quality.

CHAPTER 1: INTRODUCTION

The last modification realizing an order of magnitude improvement for a general-use analytical polarimeter was the introduction of a Faraday isolator by Gilham in 1957, subsequently re-engineered by Browne et. al. in 1997 [1, 2]. There is a need for improving the sensitivity, generality, and speed in a polarimeter by utilizing the recent advances in laser optics.

1.1 Background and Motivation

1.1.1 Pharmaceutical Application

Chiral drugs, a worldwide market in 2000 of over $120 billion in dosage form, represent more than two-thirds of all drugs under development. The realization that enantiomeric purity plays a critical role in the specificity and toxicity of pharmacological agents has prompted the *Food and Drug Administration* (**FDA**) to increase its regulatory oversight into enantiomeric purity of approved pharmaceuticals. Recent rulings by the FDA require all drugs possessing stereogenic centers to be developed as pure enantiomers.

By definition, chiral molecules display optical rotation (they rotate the plane of polarization of light, a property that is also called *optical activity*), and polarimetry is an excellent technique for search and optimization of efficient *enantioselective* processes and catalysts. However, polarimetry currently lacks several features essential for advantageous utilization in the development of chiral catalysts. Such features include: sensitivity - the best polarizers are constructed from naturally occurring calcite, which results in limited sensitivity because of its imperfect optical quality; a multi-parameter result - polarimetry currently yields only one parameter (the optical rotation) ; and high-throughput screening.

The material properties a polarimeter could simultaneously measure along with the natural optical rotation of a chiral substance are their magneto-optical effects. An optical medium subjected to magnetic field rotates the plane of polarization of light by an angle proportional to the applied magnetic field, the phenomena known as Faraday effect. The linear Faraday effect is proportional to a material parameter known as the Verdet constant, which has been extensively identified for a large number of materials.

In 1967, Graham and Raab made a theoretical prediction of high-magnetic field induced nonlinear Faraday effects, and most importantly, that the second-order dependence of optical rotation on the applied magnetic field is only exhibited by materials with natural optical activity [3]. This discovery provides for extra much-needed polarimeter measurable parameters to potentially distinguish chiral species. In chapter 2 is presented the research done in attempt to detect the second-order Faraday effect along with a substance's chirality and Verdet constant, and experimentally establish its correlation with chirality of a substance.

1.1.2 Astrobiological Application

Since Pasteur's seminal observations with enantiomers of para-tartrate over one hundred and fifty years ago, chirality has been recognized to play a critical role in living systems. Whereas natural chemical reactions rarely show chiral preference, chirality is commonplace in biological systems.

One would thus expect that the detection of chiral selectivity would be an excellent indicator for signs of life and potentially provide critical diagnostic information during space flight. Current chiral detectors such as

high pressure liquid chromatography (HPLC), gas chromatography (GC) and capillary electrophoresis (CE), while more sensitive than a polarimeter in determining chiral content, suffer from a common pitfall – they need to know the chiral compound to be measured because for measurement they need the compound specific standard. For space missions looking for signs of chirality (as a precursor for determining the presence of life), these aforementioned techniques are non-versatile and hence impractical as compared to a polarimeter, which detects chirality by measuring the polarization rotation produced by any chiral compound.

Secondly, it does not appear to have been realized that essentially any attempt to optically detect extraterrestrial chirality will be plagued by massive unwanted background due to depolarized light scattering from inevitably poor optical-quality samples. Thus, standard polarimeters, which invariably assume high optical quality, will simply not work in astrobiological applications. Indeed, it is for this reason that current polarimeters cannot even detect the relatively large density of one of the most chiral substances known – glucose – in human tissue!

The research presented in chapter 3 addresses these shortcomings, and provides a device uniquely able to sensitively detect chiral signatures in the presence of massive depolarizing scattering. Our effort takes advantage of previous work in the fields of non-invasive human glucose monitoring and bio-imaging. Most researchers in the former field consider the scattering depolarization too severe and so use unrelated phenomena (e.g., absorption spectra), and only a few have attempted to use chirality.

1.1.3 Ultrafast Application

The best current polarimeters are based on the naturally occurring crystals of calcite, which is obtainable only from natural product because

it is not yet industrially and artificially synthesized. It is required that the calcite used for making polarizers is colorless and transparent, has no bubble and no crack inside, no twin, no strain inside, and a certain size. Trials to synthesize calcite single crystal have so far been made in a variety of ways, namely, crystallization from solvent, synthesizing from gel, crystallization from flux or melt, or hydrothermal synthesis method etc, and recent floating-zone technique under high pressure. However, optical characteristics such as transparencies have not been entirely satisfactory to be industrialized due to defects such as impurities, mixing or dislocation of inclusion, or strain in crystallization inside [4-7]. Also, the growth processes developed so far are extremely slow for industrialized production. So, the polarimeters today are limited by the ever-decreasing quality of mined material.

The research presented in chapter 4 shows the development of a novel type of polarimeter based on the highly-polarization-sensitive nonlinear-optical process of harmonic generation, whose required crystals can be grown with extremely high quality. Our measurements have demonstrated an extinction ratio of 10^{-5} (roughly that of best calcite polarimeters), and a trick involving tighter phase-matching-bandwidth and lock-in detection at the second harmonic of the spectrum oscillation frequency is expected of achieving an extinction ratio better than best calcite polarizers.

CHAPTER 2: AN OSCILLATING POLARIZATION POLARIMETER

2.1 Introduction

Many diseases are still without an effective treatment today, and others have evolved resistances, requiring new therapeutic agents to be developed. Fortunately, the advent of combinatorial chemistry has helped augment the pharmaceutical industries' capacity to develop new lead compounds to treat these diseases. Optimized inhibitor structures of key enzymes in a disease often have one or more chiral centers. As the wrong enantiomers can cause harmful side effects, very high enantiomeric purity of therapeutics is essential. Due to the chiral nature of most biological components such as amino acids, sugars, or nucleotides, different enantiomers would produce different pharmacological effects. Given the importance of such chiral structures for novel therapeutic approaches, efficient syntheses are a prime priority.

Combinatorial chemistry has fundamentally changed the process by which new drugs and materials are being discovered. The combinatorial approach allows a researcher to generate up to millions of lead compounds in days or weeks, as opposed to the traditional approach of creating and testing compounds in a sequential manner. Combinatorial chemistry, when coupled with a high-throughput screening method that allows a researcher to pick desirable candidate compounds from a large library, is tremendously accelerating the pace of research.

As all chiral molecules display optical rotation (they rotate the polarization of light, a property that is also called "optical activity"), polarimetry would seem to be an excellent technique for search and optimization of efficient enantio-selective catalysts. A polarimeter can also measure the magneto-

optical effects exhibited by a material. The Verdet constant, coefficient of linear magneto-optical effect also known as the Faraday effect, is an extensively documented quantity for large number of optical materials. Also, a remarkable theoretical prediction that the second-order Faraday effect is only exhibited by chiral substances was made by Graham and Raab in 1967 [3]. Recently, large pulsed magnetic fields were used to confirm this correlation [8, 9].

The research work presented in this chapter was the development of a powerful polarimetry apparatus designed to measure the multiple optical and magneto-optical quantities. Specifically, the goal was to detect the second-order Faraday effect expected of chiral species, along with a substance's chirality and Verdet constant. A subsequent objective was to establish the correlation of the second-order Faraday coefficients to the chirality of a material.

2.2 Methods and Instruments

2.2.1 Oscillating Magnetic Field Setup

Figure 2.1 shows the beginning set-up used to investigate the non-linear Faraday effect. It is the modified polarimeter engineered by Browne et. al. inspired from the analytical polarimeter of Gilham [1, 2]. The polarimeter uses two of the state of the art techniques viz. Optical Heterodyne and Lock-in Detection into a simple Faraday effect measurement scheme. A laser beam is polarized to an initial polarization state with a polarizer. The polarized laser beam is then made to propagate through the sample medium. The sample medium is subjected to an oscillating magnetic field (amplitude B_M, frequency ω_M) coaxial to the propagating laser beam. The plane of polarization of the transmitted laser beam from the sample medium is analyzed by another polarizer, called an analyzer. A photodetector is used to extract an electrical voltage signal proportional to

the transmitted intensity through the analyzer. The spectral components of this electrical voltage signal at specific harmonics of ω_M are extracted by a lock-in amplifier.

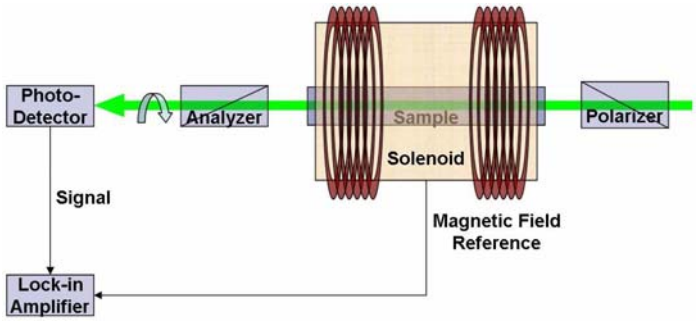

Figure 2.1: A simple oscillating polarization polarimeter setup

The analyzer is initially oriented at the transmission-minima position (crossed state with respect to the polarizer). In the absence of natural optical activity in a sample medium, the transmission minima position of the analyzer remains the same. The oscillating magnetic field causes the plane of polarization of the beam transmitted through the sample medium to oscillate about the input polarization. The transmitted intensity through the analyzer as a consequence develops oscillation at frequency $2\omega_M$, with the amplitude of intensity oscillation proportional to B_M.

Changing the orientation of the analyzer from the transmission-minima position, either manually or because of the presence of natural optical activity in a sample medium, allows some light to *leak* through the analyzer. This leaked light superposes with the signal light transmitted through the analyzer and enhances certain components of the signal, called optical heterodyne. The angular deviation θ_{LK} of the analyzer from the transmission minima orientation for any sample medium is called

leakage angle ($\theta_{LK} = 0$ at transmission-minima orientation). The transmitted intensity through the analyzer has components oscillating at various harmonics of ω_M, the amplitude of each depending upon the natural and magnetic field induced optical activity of the sample medium and the leakage angle. The sample coefficients are extracted from the amplitude measurements at these harmonics of ω_M.

2.2.2 Dual - Reference Lock-in Setup

Each spectral component of the total electrical signal at the harmonics of ω_M can be split further into its sidebands by oscillating the leakage angle (amplitude θ_L, frequency ω_L). This was achieved by introducing a *Terbium Gallium Garnet* (**TGG**) crystal faraday rotator after the polarizer (Fig. 2.2). TGG is known for its very high Verdet constant (-134 rad.$T^{-1}m^{-1}$ @ 632.8nm) and good transmission properties.

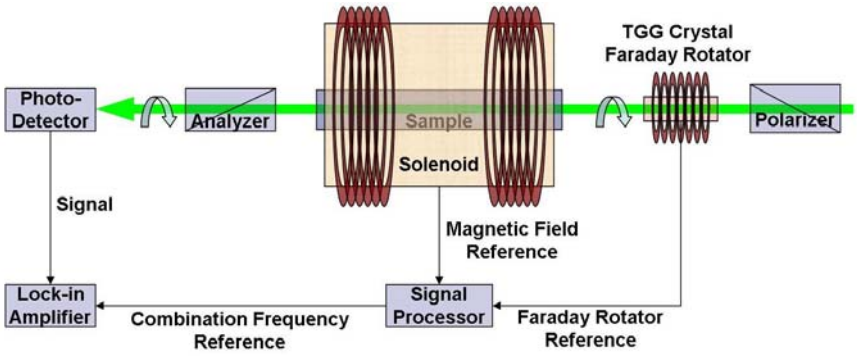

Figure 2.2: The electronic dual-reference lock-in setup

This further splitting of the signal allows further separation of the contribution to the total electrical signal by the natural and magnetic field induced optical activity of the sample medium. To retrieve all the spectral components with the lock-in amplifier, an electronic signal processor was

developed to generate the reference signals at sideband frequencies (see Appendix A: Electronic Signal Processor). The previous setup can be simplified further by acquiring the photo-detector voltage signal along with the two driving reference signals in a computer for a software-based dual-reference lock-in.

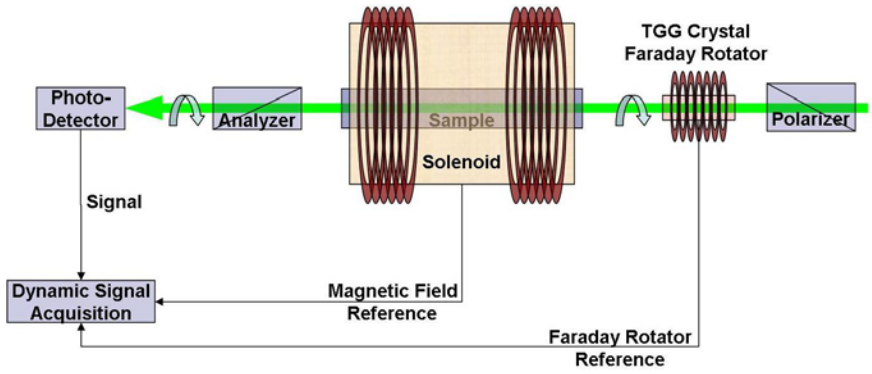

Figure 2.3: Computerized dual-reference lock-in setup

2.3 Theory

2.3.1 Optical Heterodyne

Optical Heterodyne is a powerful technique that is already used in polarization spectroscopy. Sample under study is kept between two crossed polarizers and probed with incoming polarized beam. The signal thus created by the polarization rotation is detected as intensity coming out of the crossed analyzer. Optical Heterodyne technique involves slightly uncrossing the polarizers. This allows some of the incoming beam to leak into the detector and combine coherently with the signal. This trivial change can actually improve the sensitivity by several orders of magnitude.

Consider a small amount of probe field $E_{probe}(t)$ added to the (even smaller) signal $E_{sig}(t)$. As a result, the intensity output of the analyzer as detected would be proportional to the squared magnitude of the sum of these two fields.

$$I_{det} \propto \left|E_{probe}(t)+E_{sig}(t)\right|^2$$

$$\propto \left|E_{probe}(t)\right|^2+\left|E_{sig}(t)\right|^2+2Re\left\{E_{sig}(t)E_{probe}^{*}(t)\right\} \qquad [2.1]$$

As long as the leaked probe intensity >> signal intensity, the latter can be neglected, and the output intensity reduces to

$$I_{det} \propto \left|E_{probe}(t)\right|^2+2Re\left\{E_{sig}(t)E_{probe}^{*}(t)\right\} \qquad [2.2]$$

This yields a signal proportional to $E_{sig}(t)$, which is much larger than its squared magnitude. And it also yields its phase. As long as the probe intensity is stable, there is a huge improvement in sensitivity.

2.3.2 Nonlinear Faraday Effect

Faraday Effect is the phenomenon in which the plane of polarization of a linearly polarized light propagating through a medium rotates when a magnetic field is applied in the direction of propagation. The composite natural and induced rotation $\theta_S(B)$ *per unit path length* produced by a medium under the influence of a magnetic field B can be expressed as a power series in B [3, 8-10].

$$\theta_S(B)=\alpha+\upsilon B+\beta B^2+\Gamma B^3+O(B^4) \qquad [2.3]$$

where α (deg.m^{-1}) is the natural optical activity (chirality), υ (deg.$T^{-1}m^{-1}$) is the Verdet constant, β (deg.$T^{-2}m^{-1}$) is the second order Faraday coefficient, and Γ (deg.$T^{-3}m^{-1}$) is the third order Faraday coefficient.

For small magnetic fields, the induced rotation θ is linear in field strength B and path length L, i.e. $\theta = \upsilon BL$. β and Γ arise due to the strong field Faraday Effect, wherein higher powers of B become non-negligible. Certain predictions have been made concerning the form of β and Γ and the tentative order-of-magnitude departure from field independent Verdet constant: β, like α, exists only in optically active molecules although Γ is non-vanishing for all molecules; also, the modification of the Verdet constant at high field is of the order of $1/10^6$ at fields of 10T [3].

It has already been recognized theoretically that the optically active molecules interact differently with light beams whose propagation vector **k** in the chiral medium is parallel and anti-parallel to the applied magnetic field **B** [10, 11]. The higher order effects in B have been observed unambiguously in a magnetic field of strength greater than 10T [8-10]. In non-chiral media (water), none of the non-linear effects of **B** has been observed to cause polarization rotation [8]. Measurements have been reported of the polarization rotation in liquids subjected to magnetic fields of 10T - 40T, done with pulsed technique [8, 9]. These measurements were done on enantiomers of various substances, as solvents or in solutions.

A crucial experimental observation that the sign of the value of quadratic coefficient β is same as that of chirality α of the sample is consistent with theoretical prediction that states β exists only for optically active molecules [8]. This has led to the suggestion that the parameters describing the B^2 induced change of circular birefringence should not be

called quadratic Faraday Effect; it should be considered as a quadratic dc magnetic field induced variation of natural optical rotation.

2.3.3 Jones Calculus Analysis

To analyze the beginning setup (Fig. 2.1), we use Jones calculus to calculate the output **E**-field (for a detailed calculation, please see Appendix B: NLFE Model Calculations).

Consider that the polarizer is oriented at θ_P with respect to horizontal, which sets the input **E**-field vector as

$$\vec{E}_{in} = E_0 \begin{bmatrix} \cos(\theta_P) \\ \sin(\theta_P) \end{bmatrix} \qquad [2.4]$$

The introduction of sample between the polarizer and analyzer then induces a rotation of polarization. The composite natural and induced rotation of polarization per unit path length produced by a medium under the influence of a magnetic field **B** is expressed as θ_S. The analyzer is set to pass vertically polarized component of the rotated signal field, and thus converting it into an intensity signal. The output **E**-field transmitted from the analyzer is given by

$$\vec{E}_{out} = \begin{bmatrix} 0 & 0 \\ 0 & 1 \end{bmatrix} \begin{bmatrix} \cos(\theta_S) & \sin(\theta_S) \\ -\sin(\theta_S) & \cos(\theta_S) \end{bmatrix} E_0 \begin{bmatrix} \cos(\theta_P) \\ \sin(\theta_P) \end{bmatrix} = \begin{pmatrix} 0 \\ E_0 \sin(\theta_S + \theta_P) \end{pmatrix}$$

$$\therefore \quad E_{out} = E_{in} \sin(\theta_S + \theta_P) \qquad [2.5]$$

The power transmitted through the analyzer is expressed as

$$P_{out} = P_{in} \sin^2\left(\theta_S + \theta_P\right) = P_{in} \sin^2\left(\Theta\right) \qquad [2.6]$$

where $\Theta = \theta_S + \theta_P$ is the angle (from horizontal) of instantaneous plane of polarization of the light incident upon the analyzer. Substituting for θ_S from eq. 2.3 while neglecting the contributions $O\left(B^3\right)$ to the polarization rotation, Θ becomes

$$\Theta = \theta_P + \alpha + \upsilon B + \beta B^2 \qquad [2.7]$$

We introduce $\theta_{LK} = \theta_P + \alpha$ $\left(\theta_{LK} = 0 \text{ when } \theta_P = -\alpha\right)$ to be referred as leakage, which reduces Θ to

$$\Theta = \theta_{LK} + \upsilon B + \beta B^2 \qquad [2.8]$$

The solenoid is made to generate a sinusoidal magnetic field along the solenoid's axis B $\left(= B_{amp}\cos\left(\omega_M t\right)\right)$. For small Θ, we can use the first-order small-angle sine approximation for P_{out}, which becomes

$$P_{out} = P_{in}\left(\begin{array}{l} {\theta_{LK}}^2 + \left(\frac{1}{2}\upsilon^2 + \beta\theta_{LK}\right){B_{amp}}^2 + \frac{3}{8}\beta^2{B_{amp}}^4 \\ + \left(2\upsilon\theta_{LK}B_{amp} + \frac{3}{2}\upsilon\beta{B_{amp}}^3\right)\cos\left(\omega_M t\right) \\ + \left(\left(\frac{1}{2}\upsilon^2 + \beta\theta_{LK}\right){B_{amp}}^2 + \frac{1}{2}\beta^2{B_{amp}}^4\right)\cos\left(2\omega_M t\right) \\ + \frac{1}{2}\upsilon\beta{B_{amp}}^3\cos\left(3\omega_M t\right) + \frac{1}{8}\beta^2{B_{amp}}^4\cos\left(4\omega_M t\right) \end{array}\right) \qquad [2.9]$$

Note that the signal components at the fundamental frequency ω_M and its second harmonic in the above expression vary linearly with the leakage

angle θ_{LK}. Their slope allows us to determine the values of the Verdet constant υ and the second-order faraday coefficient β of the sample medium.

The dual-reference lock-in setup (Fig. 2.2) with TGG crystal Faraday rotator further simplifies the coefficient determination by splitting the harmonics of ω_M into their sidebands separated by the leakage oscillation frequency ω_L. The Faraday rotator adds $\theta_{FR} = \theta_L \cos(\omega_L t)$ to Θ. We set $\theta_P = -\alpha$ by setting the position of the polarizer to transmission-minimum for a sample in absence of any **B**-field. The total instantaneous angle of plane of polarization of the beam incident upon the analyzer is

$$\Theta = \upsilon B_{amp} \cos(\omega_M t) + \beta {B_{amp}}^2 \cos^2(\omega_M t) + \theta_L \cos(\omega_L t) \qquad [2.10]$$

With the first-order small-angle sine approximation, P_{out} is calculated (see Appendix B: NLFE Model Calculations).

$$P_{out} = P_{in} \left(\begin{array}{l} \frac{1}{2}{\theta_L}^2 + \frac{1}{2}\upsilon^2 {B_{amp}}^2 + \frac{3}{8}\beta^2 {B_{amp}}^4 \\ +\beta \theta_L {B_{amp}}^2 \cos(\omega_L t) + \frac{1}{2}{\theta_L}^2 \cos(2\omega_L t) \\ +\frac{3}{2}\upsilon \beta {B_{amp}}^3 \cos(\omega_M t) \\ +\upsilon \theta_L B_{amp} \left(\cos((\omega_M + \omega_L)t) + \cos((\omega_M - \omega_L)t) \right) \\ +\left(\frac{1}{2}\upsilon^2 {B_{amp}}^2 + \frac{1}{2}\beta^2 {B_{amp}}^4 \right) \cos(2\omega_M t) \\ +\frac{1}{2}\beta \theta_L {B_{amp}}^2 \left(\cos((2\omega_M + \omega_L)t) + \cos((2\omega_M - \omega_L)t) \right) \\ +\frac{1}{2}\upsilon \beta {B_{amp}}^3 \cos(3\omega_M t) + \frac{1}{8}\beta^2 {B_{amp}}^4 \cos(4\omega_M t) \end{array} \right) \qquad [2.11]$$

The terms dependent on the leakage angle θ_{LK} for the various harmonics of ω_M in eq. 2.9 now feature at their respective sidebands. Note that the sidebands at $\omega_M \pm \omega_L$ and $2\omega_M \pm \omega_L$ provide a direct real-time measurement of the coefficients υ and β respectively. Another important advantage of this technique is the symmetric nature of the sidebands, which therefore also allow for a simultaneous independent verification of their measurements.

The use of small-angle sine approximation to the second-order provides a more accurate model for P_{out} when Θ is larger. However, this results in an explosion in the total number of terms in the expression for P_{out} (see Appendix B: NLFE Model Calculations). The signals at first few harmonics of the **B**-field oscillation frequency ω_M for the setup in Fig. 2.1 are:

$$P_{out}^{\omega_M} = P_{in}\left(\begin{array}{l}\left(2\upsilon\theta_{LK} - \frac{4}{3}\upsilon{\theta_{LK}}^3\right)B_{amp} + \left(\frac{3}{2}\upsilon\beta - \upsilon^3\theta_{LK} - 3\upsilon\beta{\theta_{LK}}^2\right){B_{amp}}^3 \\ -\left(\frac{5}{6}\upsilon^3\beta + \frac{5}{2}\upsilon\beta^2\theta_{LK}\right){B_{amp}}^5 - \frac{35}{48}\upsilon\beta^3{B_{amp}}^7\end{array}\right) \qquad [2.12]$$

$$P_{out}^{2\omega_M} = P_{in}\left(\begin{array}{l}\left(\frac{1}{2}\upsilon^2 + \beta\theta_{LK} - \upsilon^2{\theta_{LK}}^2 - \frac{2}{3}\beta{\theta_{LK}}^3\right){B_{amp}}^2 \\ +\left(\frac{1}{2}\beta^2 - 2\upsilon^2\beta\theta_{LK} - \beta^2{\theta_{LK}}^2 - \frac{1}{6}\upsilon^4\right){B_{amp}}^4 \\ -\left(\frac{15}{16}\upsilon^2\beta^2 + \frac{5}{8}\beta^3\theta_{LK}\right){B_{amp}}^6 - \frac{7}{48}\beta^4{B_{amp}}^8\end{array}\right) \qquad [2.13]$$

$$P_{out}^{3\omega_M} = P_{in}\left(\begin{array}{l}\left(\frac{1}{2}\upsilon\beta - \frac{1}{3}\upsilon^3\theta_{LK} - \upsilon\beta{\theta_{LK}}^2\right){B_{amp}}^3 \\ -\left(\frac{5}{12}\upsilon^3\beta + \frac{5}{4}\upsilon\beta^2\theta_{LK}\right){B_{amp}}^5 - \frac{7}{16}\upsilon\beta^3{B_{amp}}^7\end{array}\right) \qquad [2.14]$$

More terms in the above expressions for individual frequency components of P_{out} show linear or higher-order dependence on the leakage angle θ_{LK}. These terms can be further separated by the dual-reference lock-in setup.

2.4 Results

The oscillating polarization polarimeter (Fig. 2.1) was constructed with a 100mW laser beam sourced from a Coherent Verdi laser (continuous-wave output at λ = 532nm). Glan-Thompson Calcite polarizers (measured extinction-ratio of 10^{-6}) were used to obtain best polarization sensitivity.

The axial magnetic field oscillations were achieved with a Helmholtz coil, driven by a sinusoidal current source. The maximum amplitude of driving current used was 750mA (manufacturer suggested maximum operating current), which generated B_{amp} = 2.3mT, at the driving frequency ω_M = 900Hz. Later, the magnetic field strength in our setup was increased to B_{amp} = 80mT by using a concatenated set of 4 Solen Hepta-litz solenoid coils (30mH each) to form a longer solenoid, resonantly driven at substantially higher currents (I_{amp} = 4.5Amps at 650 Hz).

A Thorlabs DET110 photodetector was used in photo-conducting mode to output electric current proportional to the incident transmitted power from the analyzer. The output current was converted into voltage signal determined by the detector responsivity (0.3 Amp/W for λ = 532nm) and the load resistance (Eq. 2.15). A digital lock-in amplifier (SR830, from Stanford Research Systems) was then utilized for signal extraction.

$$\text{Signal} = P_{out}\ \text{Responsivity}(\lambda)\ R_{Load} \qquad [2.15]$$

Saturation of photodetector introduces unwanted higher harmonics of an oscillating signal and thus distorts the measurements. The load resistance on a photodetector, aside from setting the amplification factor, also changes the saturation intensity of a photodetector (Fig. 2.4).

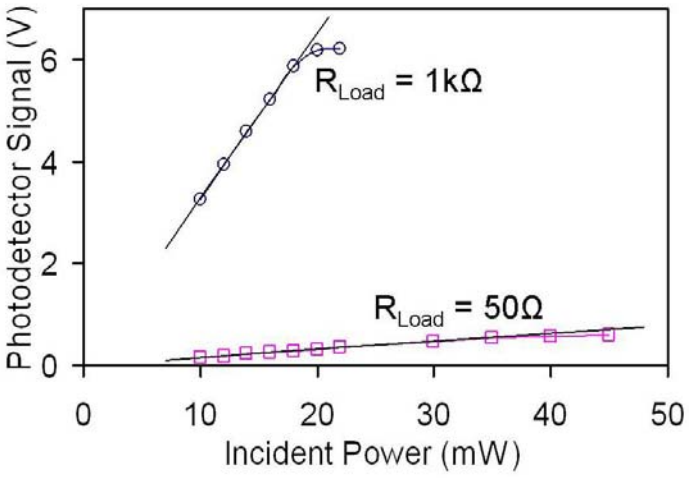

Figure 2.4: Thorlabs photodetector DET110 response vs. incident power for different load resistances. Larger load resistance saturates the photodetector at lower incident power. The slope is a measure of the amplification factor (V/Amp).

The second-order Faraday effect, theoretically predicted to be correlated to the natural optical activity of a substance, is expected to show stronger signature for substances with higher chirality. Among chiral compounds, Glucose and its enantiomer Fructose molecules have some of the highest known specific optical rotations ($[\alpha]_D^{24}$ (Glucose) = 52.5°, $[\alpha]_D^{24}$ (Fructose) = -92°). These readily available members of the sugar family are thus the best candidates to experimentally discover and characterize the second-order Faraday effect.

To ensure the linearity of polarimeter response with input power, the polarimeter was tested at two input power levels 20mW and 40mW (Fig. 2.5). The signal strength was expected to double with twice the input

power. The dominating **B**-field term in lock-in signals at frequencies ω_M and $2\omega_M$ was verified from measurements done at two different **B**-fields (Fig. 2.6), B_{amp} = 40mT and 80mT. The lock-in signal amplitude at ω_M was expected to double (dominating term is proportional to B_{amp}), whereas the signal amplitude at $2\omega_M$ was expected to quadruple (dominating term is proportional to B_{amp}^2) as a result of applying twice as strong B_{amp}.

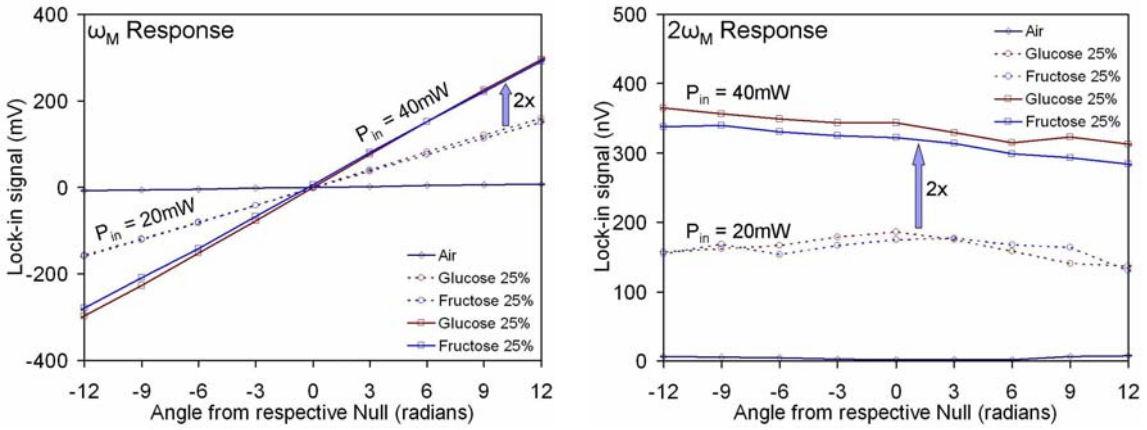

Figure 2.5: Measured lock-in signal amplitudes at different harmonics of ω_M for 20mW and 40mW input power.

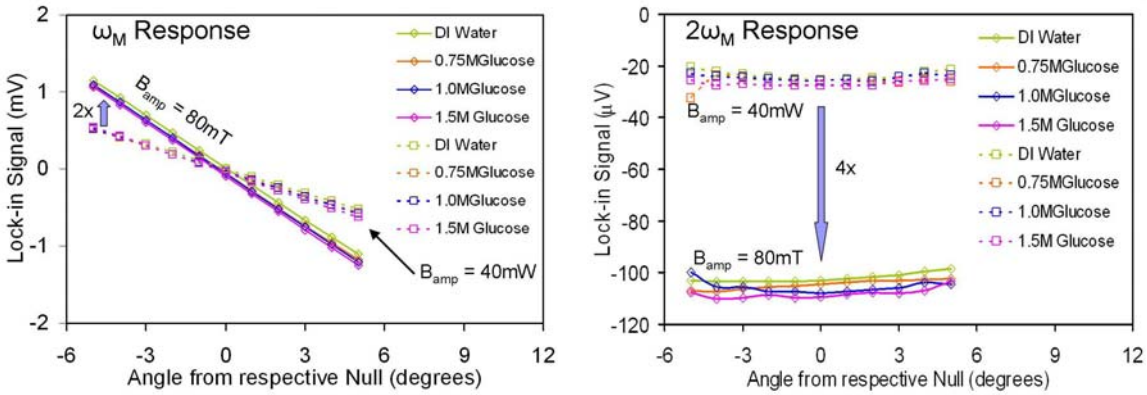

Figure 2.6: Measured lock-in signal amplitudes at different harmonics of ω_M for two magnetic fields. The dashed curves represent signal amplitudes for B_{amp} = 40mT, while the solid curves represent signal amplitudes for B_{amp} = 80mT.

The lock-in signal and phase at harmonics ω_M and $2\omega_M$ were measured for water solutions of different concentrations of Glucose and Fructose (Fig. 2.7). Polarimeter measurements were also done with solutions of Glucose and Fructose mixed together in different proportions, which exhibit a natural optical rotation proportional to their ratio, to investigate the effect of simultaneous presence of different enantiomers (Fig. 2.8).

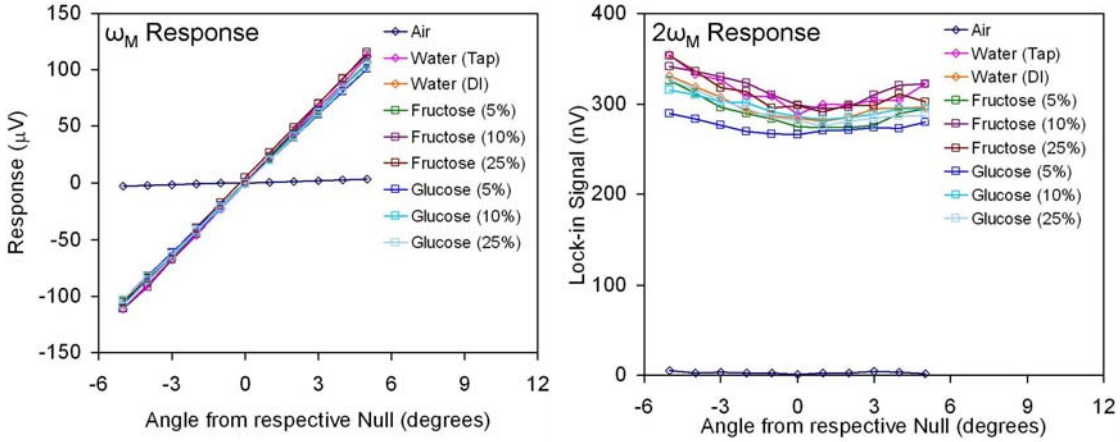

Figure 2.7-(left and right): Lock-in signals measured at solenoid frequency ω_M, and $2\omega_M$ for solutions with different concentrations Glucose and Fructose.

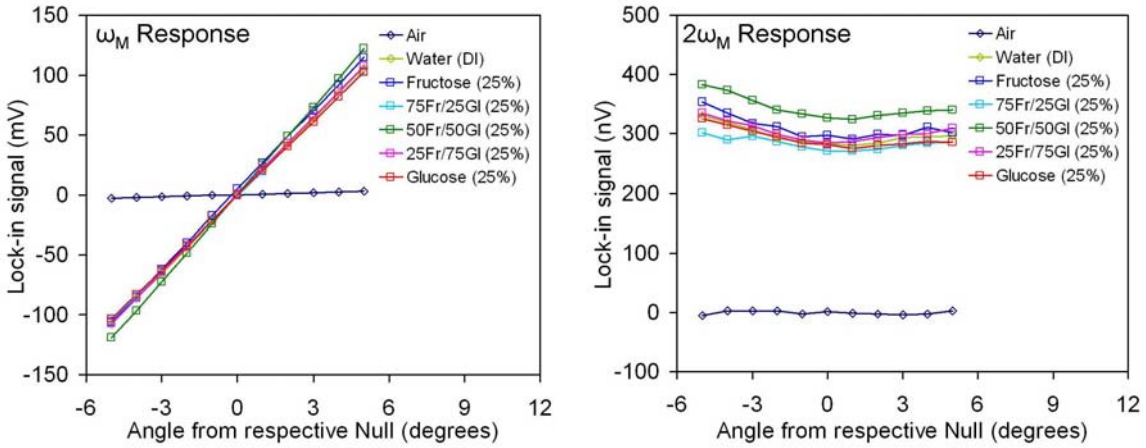

Figure 2.8: Measured lock-in signals at ω_M and $2\omega_M$ for solutions of Glucose and Fructose mixed in different proportions.

2.5 Discussion

The lock-in amplitudes at frequencies ω_M for various glucose and fructose solutions showed an expected strong linear dependence on the leakage angle (Fig. 2.5 - Fig. 2.8, eq. 2.9, 2.12). The lock-in amplitudes at frequencies $2\omega_M$ for various glucose and fructose solutions, and their mixes, remained relatively constant with any change in the leakage angle (Fig. 2.5 - Fig. 2.8). The expected linear dependence on leakage angle due to a substance's β was not recognized in the $2\omega_M$ responses (eq. 2.9, 2.13).

The results overwhelmingly showed no appreciable change upon changing the concentration of chiral substances, or the prevalent enantiomer. The close proximity to water signified that water's high Verdet constant (278°/(Tm) for 532nm [12]) masks the behavior of the chiral solute. Also, the B_{amp} available in our current setup was still small to magnify the nonlinear Faraday effect terms for overcoming the unavoidable huge Verdet terms background of water.

To suppress the background caused by the large Verdet constant of water in our measurements, solvents with approximately zero Verdet constant were searched for, without any promising results. Separately, it was found in the literature that certain water-soluble salts of iron and copper, such as $FeCl_3$ and $CuSO_4$, exhibit a negative Verdet constant that can be used to reduce the effective Verdet constant of a water solution. Solutions of different concentrations of copper sulfate were measured with the polarimeter. The contribution of the Verdet constant terms to signals at various harmonics of ω_M get dramatically reduced with increasing concentrations of copper sulfate (Fig. 2.9). However, to achieve a solution of copper sulfate with water with zero effective Verdet constant required a high concentration (>1.5M), causing crystallization in the solution of the

solute because of saturation. This effectively defeated the use of this approach.

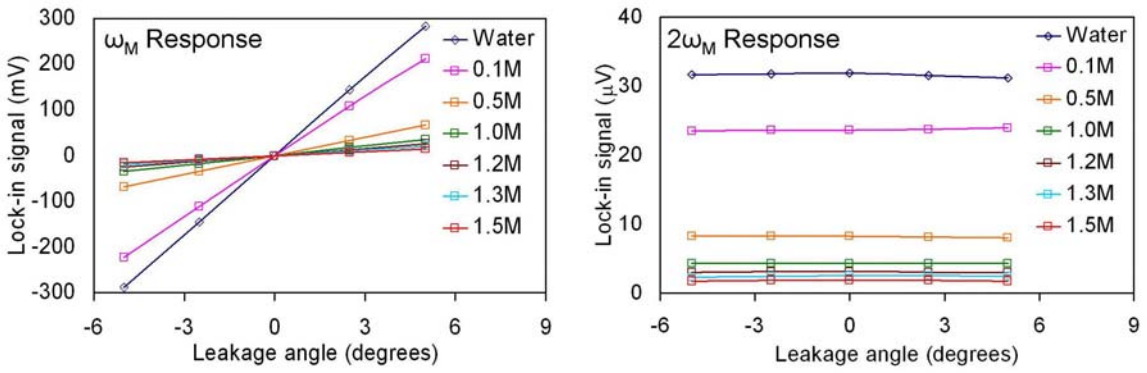

Figure 2.9: Polarimeter measurements of solutions with different concentrations of copper sulfate, a negative Verdet constant salt. Increasing concentrations of copper sulfate decreased the effective Verdet constant of the solution.

Other approaches were developed to externally subdue the effect of water. First approach made the use of negative Verdet constant crystals, such as TGG, to externally reduce the overall Verdet constant of the crystal and the sample solution. The length of the crystal is determined by the crystal position in the solenoid to perfectly reduce the Verdet constant to zero. Another approach was to use a longer crystal and the exact amount of compensation of Verdet constant is controlled by positioning it along the axis of the solenoid because **B**-field strength varies along the axis of a finite solenoid. This approach reduced the Verdet constant dominated lock-in signal at ω_M by 3 orders of magnitude. Since the contribution of the signal at frequency ω_M to the overall signal was found orders of magnitude higher than signal components at other harmonics of ω_M, reduction of the signal amplitude at ω_M lowered the overall signal, and thus allowed for further amplification of the obtained overall signal.

Using the TGG crystal to subdue the effect of high Verdet constant of water as mentioned above, solutions of Glucose and Fructose were measured with the dual-reference lock-in polarimeter (Fig. 2.10). The lock-in signal amplitudes measured at the sideband frequencies $2\omega_M \pm \omega_L$ $(2 \text{ x } 650 \pm 90)$ were expected to be equal to each other, and proportional to the second-order faraday coefficient.

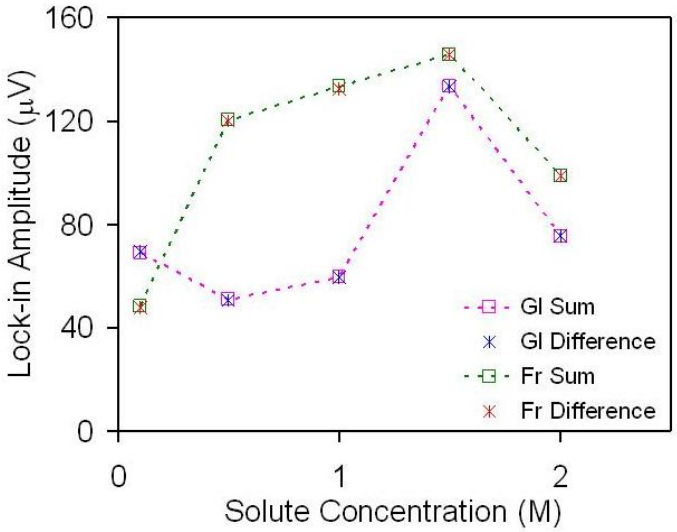

Figure 2.10: Lock-in amplitude measured at frequency sidebands $2\omega_M + \omega_L$ and $2\omega_M - \omega_L$ for solutions with different concentration of Glucose and Fructose.

The above measurements didn't show a linear increase in the signal amplitude with increasing concentrations of chiral solutes - the necessary conclusive evidence of observation of β induced rotation. The above data are thus simply understood as noise contributed from spurious electrical signals in components, and sample response to noise in driving current.

CHAPTER 3: A ROTATING POLARIZATION POLARIMETER

This chapter awaits presentation and publication by the author in:

[1] N.Kothari, A.Jafarpour, R.Trebino, T.L.Thaler and A.S.Bommarius, "Astrobiological Polarimeter", under review in Journal of Astrobiology, Mar 2007

[2] N.Kothari, A.Jafarpour, R.Trebino, T.L.Thaler and A.S.Bommarius, "Astrobiological Polarimeter", presenting to SPIE conference on Optics and Photonics 2007, San Diego, CA, Aug 2007

[3] N.Kothari, A.Jafarpour, R.Trebino, "Rotating Polarization Polarimeter", presenting to OSA conference Frontier in Optics 2007, San Jose, CA, Sep 2007

3.1 Life, Chirality, and Its Measurement

Since Pasteur's seminal observations with enantiomers of tartrate over one hundred and fifty years ago, chirality has been recognized to play a critical role in biological systems. Whereas the chemistry of inanimate systems rarely shows chiral preference, chirality is commonplace, and often quite strong, in biological systems. Thus, the detection of chirality is an excellent indicator of extra-terrestrial life [13, 14].

For terrestrial use, polarimeters are quite common, all essentially comprising pairs of crossed polarizers with assorted modulators and detectors [15-18]. However, little effort has been devoted to polarimeters for astrobiological purposes during space exploration. We know of only one such effort–the "SETH-Cigar" developed in Europe for Mars and other extra-terrestrial destinations and comprises a carefully engineered compact pair of crossed polarizers [14].

Unfortunately, naturally occurring samples, on earth and elsewhere, whether living or non-living, exhibit significant *depolarizing light scattering*

(**DLS**). DLS occurs because naturally occurring matter is structurally complex, with many tiny regions of different refractive indices and absorption coefficients. In addition to scattering the beam, these individual regions absorb, reflect, refract, or phase-delay orthogonal polarizations by different amounts, all of which change the intensity and polarization state of each small spatial region of a light wave by a random amount. DLS does not require that the medium or its small sub-regions have any birefringence or dichroism (the tendency for one polarization to be absorbed more than its orthogonal counterpart), both of which are well known to rotate polarization, although, of course, these properties induce additional depolarization. A light ray propagating through a large number of such tiny regions evolves to an essentially random polarization state (Fig. 3.1).

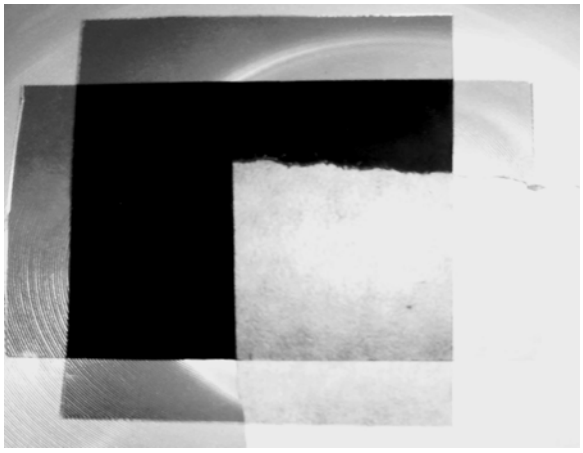

Figure 3.1: A piece of wax paper (lower right) held between crossed polarizers depolarizes the light and causes significant light to pass through the second polarizer.

Thus a light beam experiencing significant DLS develops an extremely complex polarization distribution in space. See, for example, Fig. 3.2, which shows a significant decrease in the measured *extinction ratio* (**ER**, the ratio of light transmitted when the polarizers are crossed to that when

they are parallel, and the measure of the quality of a polarimeter) with increased DLS. As a result, the performance of conventional polarimeters deteriorates badly in the presence of DLS [19, 20].

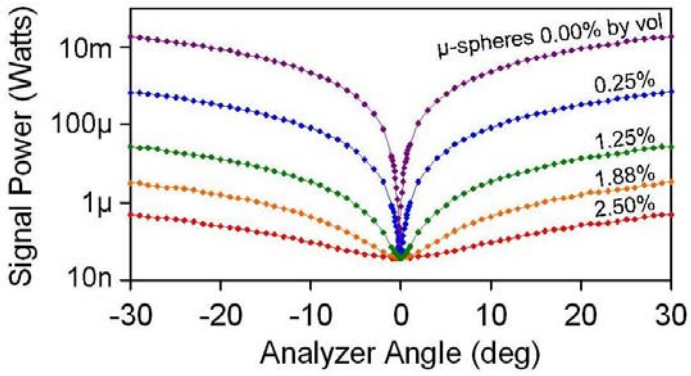

Figure 3.2: Light power transmitted by a polarizer-analyzer pair vs. analyzer angle for several concentrations of 10-µm polystyrene micro-spheres added to water. The extinction ratio (ER) is the ratio of the minimum and maximum transmitted powers on a given curve. The 10-µm polystyrene micro-spheres introduce DLS through their surface reflections (they are neither birefringent nor dichroic). Increasing the concentration of micro-spheres significantly increases the DLS and deteriorates the ER of conventional polarimeters and hence significantly reduces its ability to accurately determine chirality.

Consequently, conventional polarimeters require the user to carefully prepare "optically clean" samples, that is, samples essentially free of such structure and its resulting DLS. This means the removal of essentially all particulate matter from the sample surface and interior—something utterly impractical in extra-terrestrial environments. Thus, conventional polarimeters are ineffective for astrobiological applications.

To appreciate this problem – in a very terrestrial setting – consider attempting to determine whether a *human* is a living organism solely by detecting his chirality using a conventional polarimeter. This would seem a simple problem in view of a typical human's significant amount, ~ 1g/ℓ, of glucose, a molecule with one of the highest known specific optical

rotations ($[\alpha]_D^{24} = 52.5^o$). Unfortunately, the extremely high DLS in human tissue completely depolarizes the light beam of the conventional polarimeter, and so it fails for such a sample: its extinction coefficient approaches unity.

With this example in mind, we may note that the problem of detecting astrobiological chirality bears a striking resemblance to the problem of developing a chirality-based non-invasive human glucose monitor for diabetics, who must frequently monitor their glucose levels. Both applications require a lightweight, compact, power-efficient, and robust polarimeter, and both require the measurement of chirality in the presence of significant amounts of DLS [21-28]. In fact, the non-invasive human-glucose monitoring problem is actually more difficult: it also requires low-cost manufacturability, specificity for glucose, and approximately 5% accuracy. No such stringent conditions are required for a chirality monitor for astrobiological applications, where only a few devices will be constructed, any chiral substance would be interesting, and an order-of-magnitude result would suffice. Unfortunately, a chirality-based non-invasive human-glucose monitor remains an unsolved problem [29]. Much effort has been expended on it, however, and astrobiology would benefit from the experience of this disparate community [29-34].

So, for astrobiological applications, we have investigated a polarimeter inspired by a chirality monitor developed (but later abandoned due to insufficient accuracy [35]) for non-invasive *in vivo* human-glucose sensing [36-39]. In our polarimeter, we continuously rotate the plane of linear polarization of a laser beam before passing it through a sample with DLS, which we then analyze with a fixed-orientation analyzer, which generates a sinusoidal voltage signal. We compare this signal with a voltage signal for an analogous set up without a sample. If the sample medium is chiral, it further rotates the (linear) polarization of the beam, introducing a phase

difference between its sinusoidal output voltage and that of the reference beam, and this phase difference indicates the sample chirality.

3.2 Methods and Instruments

3.2.1 Conventional Polarimeters

Polarimeters determine the chirality of a sample medium by measuring the amount of polarization rotation induced by a sample on the light propagating through it. If one linear polarizer generates a purely linear polarization, the transmittance T of a second linear polarizer (called an analyzer) is given by Malus law, $T = \cos^2(\delta)$, where δ is angle between the plane of polarization of incident linearly polarized light and the transmission axis of the analyzer. The sample medium causes rotation of the polarization by an angle α proportional to the sample's chirality. The determination of chirality requires finding the *phase shift* generated in the transmitted intensity sinusoid upon introduction of a chiral sample (Fig. 3.3), by rotating the analyzer to the new angle of minimum transmission.

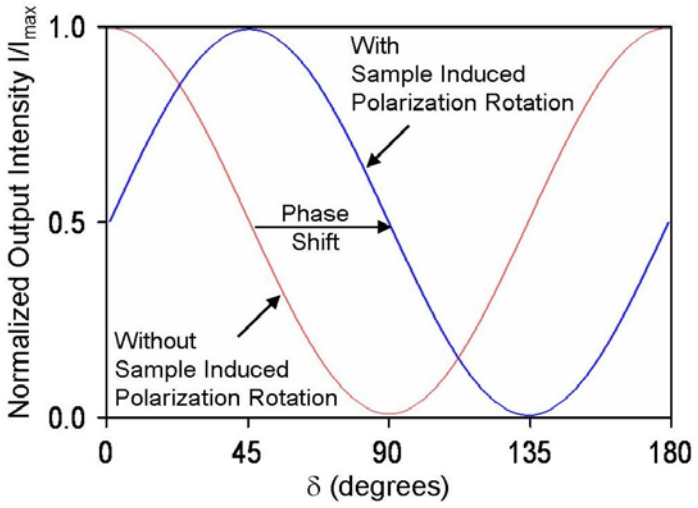

Figure 3.3: Transmittance of a linear polarizer (from Malus law) expressed as normalized output intensity (I/Imax) vs. δ, the angle between the incident plane of polarization and the transmission axis of the polarizer.

Conventional polarimeters simply use a good set of polarizers (ER ~10^6:1) and a photo-detector that allows for a quantitative measurement of intensity to determine α [40]. Recently proposed polarimetry techniques utilize polarization- or intensity-modulated input light, optical heterodyne detection, advanced electronics, and post-measurement data processing with lock-in detection techniques to determine the polarization rotation with higher sensitivity [41-44].

Polarimeters based on modulating the input polarization (i.e. the optical phase) generally dither the instantaneous linear polarization by a few degrees about a mean linear polarization. The signal amplitudes measured at various harmonics of the modulation frequency are then used to determine the sample-induced polarization rotation. Some techniques require measurements for different mean linear polarizations. However, essentially all of these techniques deteriorate badly in the presence of DLS, which depolarizes the light and hence severely reduces the amplitude of the output signal-voltage sinusoid.

3.2.2 The Rotating Polarization Polarimeter

In 1992, Cote et al. proposed a true phase-shift measurement technique that overcomes the amplitude noise effects [45]. In this chapter, we further investigate this technique for its potential of overcoming significant DLS. It involves lock-in detection of the output voltage signal *phase* (not its *amplitude*) of a *rotating* linear polarization relative to a rotating linear reference polarization, and is described in the next section. We will refer to it as the *rotating-polarization* (**RP**) polarimeter. Cote, et al. achieved a rotating linear polarization by using a linear polarizer and a *quarter-wave plate* (**QWP**) to first yield a circularly polarized beam and then used a

rotating linear polarizer. While this sequence of optics allows the use of multiple wavelengths (polarizers are broadband), it results in the loss of half of the intensity of light provided by the first polarizer. We use instead a linear polarizer and rotating a QWP/mirror combination (effectively a half-wave plate), which minimizes the intensity loss in the process yielding a more energy-efficient device.

While DLS decreases both the dc- and ac-components of the transmitted light and voltage signals, it does not affect the phase difference induced by chirality. A lock-in amplifier then extracts the necessary relative phase between the signal and reference voltage sine waves. This detection apparatus can see a sine wave component buried in over 100 dB of noise. The experimental set-up is illustrated in Fig. 3.4.

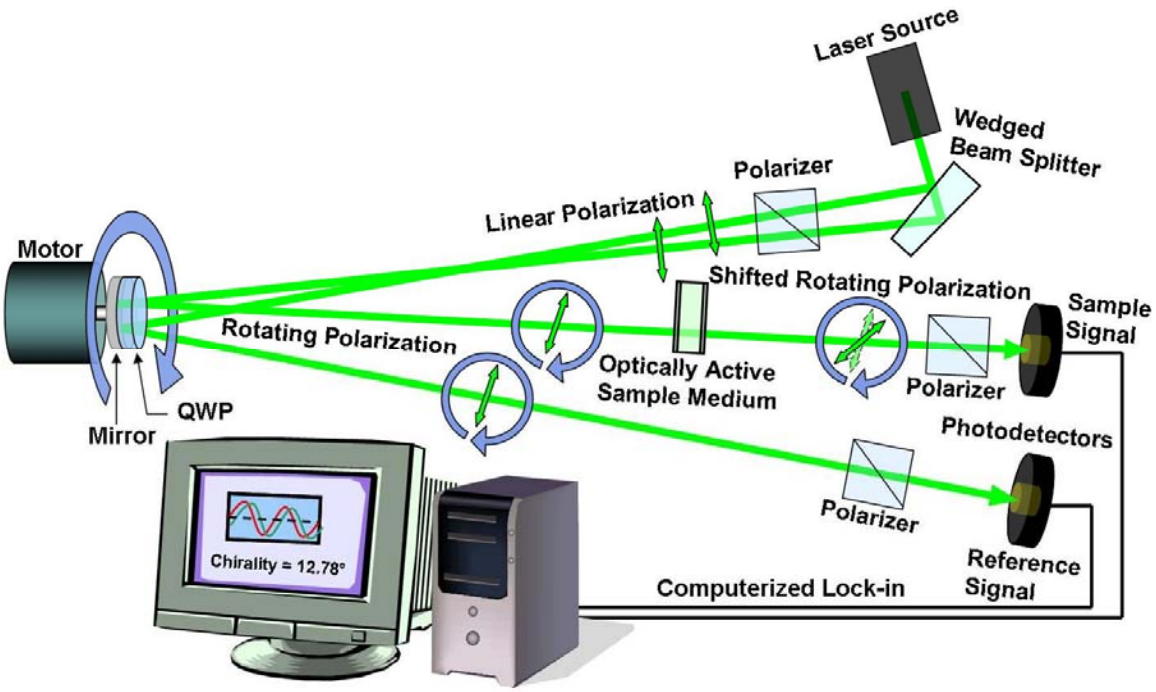

Figure 3.4: Rotating polarization polarimeter set-up.

3.3 Theory

3.3.1 Jones Calculus Analysis

For simplicity, we first use Jones calculus to describe the effect of each optical component on the E-field of the transmitted light and derive an expression for the output light signal and retrieve the polarization rotation of an optically clean sample [46]. Since Jones calculus can only be used for fully polarized light without a depolarized component, we subsequently account for depolarization effects in samples with DLS using more complex Mueller matrices, which can account for an incoherent component due to DLS.

In this analysis, we assume that the samples do not exhibit any circular dichroism or absorption at the experimental wavelength, so we ignore these effects.

A collimated laser beam is split into two and both beams are passed through a polarizer to create two vertically polarized beams, which act as the reference and sample signal beams. The E-fields for both beams have the following Jones vectors:

$$E_{\text{Reference Beam}} = E_{in}\begin{bmatrix}0\\1\end{bmatrix};\ E_{\text{Sample Beam}} = E_{in}\begin{bmatrix}0\\1\end{bmatrix} \qquad [3.1]$$

A zero-order QWP with a mirror on its back then acts as a *half-wave plate* (**HWP**) rotating the polarization of both the beams by an identical amount: 2θ, where θ is the rotation angle of the QWP. Mechanically rotating the QWP/mirror at a frequency ω then rotates the polarization of the two beams at twice the mechanical frequency, 2ω. Since θ = ωt, the Jones matrix for combination of QWP oriented at an angle θ from vertical and the

mirror, and the resultant Jones vectors for the reference and signal beam with rotating polarizations are:

$$\text{Rotating}_{\text{QWP,Mirror}} = e^{i\frac{\pi}{2}}\begin{bmatrix}\cos(2\omega t) & -\sin(2\omega t)\\ \sin(2\omega t) & \cos(2\omega t)\end{bmatrix} \qquad [3.2]$$

$$E^{\text{Rotating}}_{\text{Reference Beam}} = \text{Rotating}_{\text{QWP,Mirror}} \bullet E_{in}\begin{bmatrix}0\\1\end{bmatrix} = E_{in}e^{i\frac{\pi}{2}}\begin{bmatrix}-\sin(2\omega t)\\ \cos(2\omega t)\end{bmatrix} \qquad [3.3]$$

$$E^{\text{Rotating}}_{\text{Sample Beam}} = E_{in}e^{i\frac{\pi}{2}}\begin{bmatrix}-\sin(2\omega t)\\ \cos(2\omega t)\end{bmatrix} \qquad [3.4]$$

The reference beam then propagates through a vertical polarizer to a photo-detector that produces a sinusoidal voltage signal, $V_{\text{Reference}}$.

$$E^{\text{Output}}_{\text{Reference Beam}} = \begin{bmatrix}0 & 0\\ 0 & 1\end{bmatrix} \bullet E^{\text{Rotating}}_{\text{Reference Beam}} = E_{in}e^{i\frac{\pi}{2}}\begin{bmatrix}0\\ \cos(2\omega t)\end{bmatrix} \qquad [3.5]$$

$$\because \text{Intensity}^{\text{Output}}_{\text{Reference Beam}} \propto \left|E^{\text{Output}}_{\text{Reference Beam}}\right|^2$$

$$\therefore V_{\text{Reference}} \propto \text{Intensity}^{\text{Output}}_{\text{Reference Beam}} \propto \cos^2(2\omega t) = \frac{1}{2}\cos(4\omega t) + \frac{1}{2} \qquad [3.6]$$

The sample signal beam propagates through the sample medium, which rotates the plane of polarization of the beam by an angle α proportional to the chirality of the sample medium. Consequently, the plane of polarization of the signal beam still rotates at the same frequency 2ω, but due to sample chirality, it now develops a *phase difference* α with respect to the reference beam. The signal beam then propagates through a

polarizer to the photo-detector, which then produces a phase-shifted voltage signal, V_{Sample}.

$$E^{Output}_{Sample\ Beam} = \begin{bmatrix} 0 & 0 \\ 0 & 1 \end{bmatrix} \begin{bmatrix} \cos(\alpha) & -\sin(\alpha) \\ \sin(\alpha) & \cos(\alpha) \end{bmatrix} \bullet E^{Rotating}_{Sample\ Beam} \quad [3.7]$$

$$\therefore E^{Output}_{Sample\ Beam} = E_{in} e^{i\frac{\pi}{2}} \begin{bmatrix} 0 \\ \cos(2\omega t + \alpha) \end{bmatrix} \quad [3.8]$$

$$\because Intensity^{Output}_{Sample\ Beam} \propto \left| E^{Output}_{Sample\ Beam} \right|^2$$

$$\therefore V_{Sample} \propto Intensity^{Output}_{Sample\ Beam} \propto \cos^2(2\omega t + \alpha) = \frac{1}{2}\cos(4\omega t + 2\alpha) + \frac{1}{2} \quad [3.9]$$

The reference and sample voltage signals are then processed by a computerized lock-in detector, which measures the phase difference Φ between the sample and reference voltage signal waves at frequency 4ω, which represents the polarization rotation ($\Phi = 2\alpha$ as evident from expressions for $V_{Reference}$ and V_{Sample}).

3.3.2 Mueller Matrix Analysis

The preceding analysis assumes that the sample introduces only optical rotation, and does not exhibit any DLS. Now we examine the effect of DLS. Multiple scattering is an extensively studied phenomenon in, for example, the bio-imaging community[47, 48]. Multiple scattering in the Rayleigh regime (when the size of scattering particles is much smaller, ~ 1/10th or less, than the wavelength of scattered radiation) and the Mie regime (scattering by larger particles) is characterized through the complex Mueller matrix for emerging radiation in the forward-scattering as

well as back-scattering direction[49-52]. The transmitted beam from a sample with DLS has both ballistic (i.e. unscattered, hence polarized) and incoherent (i.e, scattered, hence depolarized) components. In the rotating-polarization polarimeter, the incoherent (depolarized) component of light contributes a DC signal while also reducing the signal strength (intensity and therefore the voltage amplitude) of the AC polarized component, which still rotates at the same frequency, with its phase shifted by an amount equal to the chirality of the sample.

The above effects are described by Mueller matrices as follows. The Stokes vector describing both the vertically polarized input sample and reference beams are:

$$S_{\text{Reference Beam}} = S_0 \begin{bmatrix} 1 \\ 1 \\ 0 \\ 0 \end{bmatrix};\ S_{\text{Sample Beam}} = S_0 \begin{bmatrix} 1 \\ 1 \\ 0 \\ 0 \end{bmatrix} \qquad [3.10]$$

The reference and sample beams propagate through the QWP/mirror combination (effectively a HWP) rotating at a frequency ω. The Mueller matrix that describes the QWP/mirror combination rotating at a frequency ω and the resultant Stokes vectors for the reference and signal beam with rotating polarization are:

$$\text{Rotating}_{\text{QWP/Mirror}} = \begin{bmatrix} 1 & 0 & 0 & 0 \\ 0 & \cos(4\omega t) & \sin(4\omega t) & 0 \\ 0 & -\sin(4\omega t) & \cos(4\omega t) & 0 \\ 0 & 0 & 0 & 1 \end{bmatrix} \qquad [3.11]$$

$$S^{\text{Rotating}}_{\text{Reference Beam}} = \text{Rotating}_{\text{QWP/Mirror}} \cdot S_0 \begin{bmatrix} 1 \\ 1 \\ 0 \\ 0 \end{bmatrix} = S_0 \begin{bmatrix} 1 \\ \cos(4\omega t) \\ -\sin(4\omega t) \\ 0 \end{bmatrix} \qquad [3.12]$$

$$S^{\text{Rotating}}_{\text{Sample Beam}} = S_0 \begin{bmatrix} 1 \\ \cos(4\omega t) \\ -\sin(4\omega t) \\ 0 \end{bmatrix} \quad [3.13]$$

The reference beam propagates through a vertical analyzer to the photodetector, resulting in an output Stokes vector, $S_{\text{Output Reference Beam}}$.

$$S^{\text{Output}}_{\text{Reference Beam}} = \frac{1}{2} \begin{bmatrix} 1 & -1 & 0 & 0 \\ -1 & 1 & 0 & 0 \\ 0 & 0 & 0 & 0 \\ 0 & 0 & 0 & 0 \end{bmatrix} \cdot S^{\text{Rotating}}_{\text{Reference Beam}} \quad [3.14]$$

$$\therefore \; S^{\text{Output}}_{\text{Reference Beam}} = \frac{1}{2} S_0 \left(1 - \cos(4\omega t)\right) \begin{bmatrix} 1 \\ -1 \\ 0 \\ 0 \end{bmatrix} \quad [3.15]$$

The Mueller matrix (M_{Sample}) that describes a chiral sample medium, which also exhibits DLS, can be expressed as the sum of a non-scattering polarization-rotating matrix and a scattering depolarizing matrix. These individual matrices describe the effect of a scattering chiral sample medium on the input radiation. Specifically, the ballistic (unscattered) light only undergoes polarization rotation, and constitutes the non-depolarized rotation matrix. On the other hand, multiply scattered light (in the forward direction) becomes completely depolarized and incoherent. We represent the ballistic light contribution to the normalized total signal by β, so the contribution of depolarized component is (1-β):

$$M_{Sample} = \beta \begin{bmatrix} 1 & 0 & 0 & 0 \\ 0 & \cos(2\alpha) & \sin(2\alpha) & 0 \\ 0 & -\sin(2\alpha) & \cos(2\alpha) & 0 \\ 0 & 0 & 0 & 1 \end{bmatrix} + (1-\beta) \begin{bmatrix} 1 & 0 & 0 & 0 \\ 0 & 0 & 0 & 0 \\ 0 & 0 & 0 & 0 \\ 0 & 0 & 0 & 0 \end{bmatrix} \quad [3.16]$$

$$\therefore \; M_{Sample} = \begin{bmatrix} 1 & 0 & 0 & 0 \\ 0 & \beta\cos(2\alpha) & \beta\sin(2\alpha) & 0 \\ 0 & -\beta\sin(2\alpha) & \beta\cos(2\alpha) & 0 \\ 0 & 0 & 0 & \beta \end{bmatrix} \quad [3.17]$$

The sample beam propagates through the sample medium that also exhibits DLS and then a vertical analyzer to the photodetector, resulting in a voltage signal that is proportional to $S_{\text{Output Sample Beam}}$.

$$S^{\text{Output}}_{\text{Sample Beam}} = \frac{1}{2} \begin{bmatrix} 1 & -1 & 0 & 0 \\ -1 & 1 & 0 & 0 \\ 0 & 0 & 0 & 0 \\ 0 & 0 & 0 & 0 \end{bmatrix} \cdot M_{Sample} \cdot S^{\text{Rotating}}_{\text{Sample Beam}} \quad [3.18]$$

$$\therefore \; S^{\text{Output}}_{\text{Sample Beam}} = \frac{1}{2} S_0 \left(1 - \beta\cos(4\omega t + 2\alpha)\right) \begin{bmatrix} 1 \\ -1 \\ 0 \\ 0 \end{bmatrix} \quad [3.19]$$

Analyzing the Stokes vectors for the output beams confirms that the phase difference between the two signals is the same 2α as in the case of no DLS at frequency 4ω. Therefore, the RP polarimeter appears to be an excellent method for measuring rotation induced by a chiral sample, undeterred by DLS.

3.4 Results

The rotating polarization polarimeter (Fig. 3.4) was constructed with two 15mW laser beams sourced from a Coherent Verdi laser (continuous-wave output at λ = 532nm). Glan-Thompson Calcite polarizers (measured extinction-ratio of 10^{-6}) were used to obtain best polarization sensitivity. A zero-order QWP and high-reflective mirror were stacked together in a mount, which was mounted on the axle of a Maxxon model-airplane mini-motor. The rotation speed of the motor was computer adjustable and monitored. Both the sample and reference beams were made to travel almost parallel to each other (angle of deviation less than 3°) to ensure confinement to the acceptance angles of the polarizers and QWP.

Two Thorlabs DET110 photodetector were then used in photo-conducting mode to obtain current signals linearly dependent on the incident power. The reference current signal was transformed into a voltage signal by a fixed load resistance. The sample current signal was transformed into a voltage signal using a variable amplification trans-impedance amplifier. A computerized lock-in was then utilized for signal extraction.

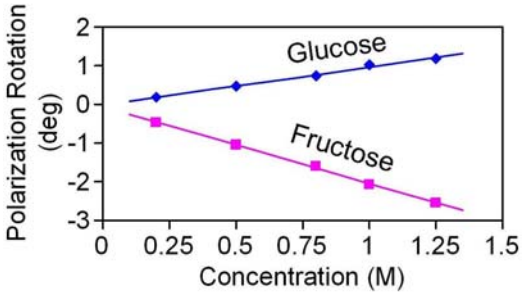

Figure 3.5: The rotating polarization polarimeter measurements of polarization rotation of samples with increasing concentrations of glucose and fructose.

We demonstrated that the RP polarimeter works in the absence of DLS by measuring several optically clean samples with varying concentrations of glucose and fructose. The measured polarization rotation changed linearly upon varying the concentration of chiral solutes Glucose and Fructose (Fig. 3.5). The accuracy of these measurements was verified by comparing them with the measurements from a commercial polarimeter.

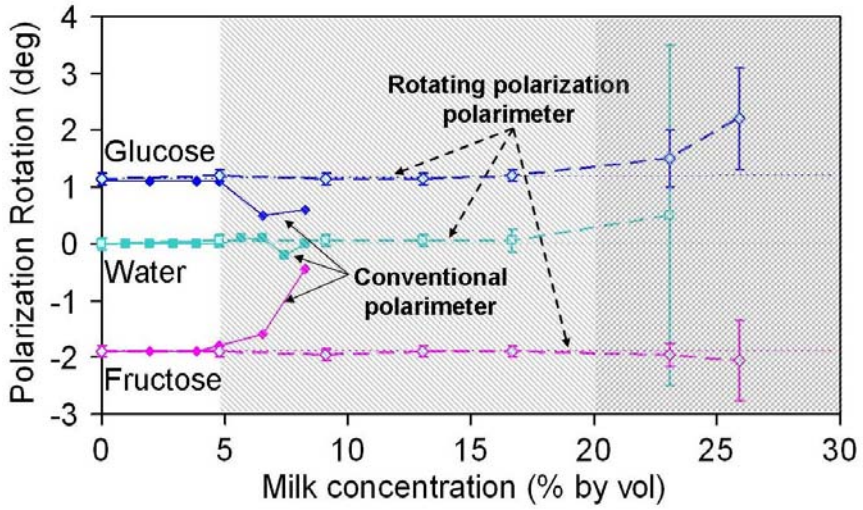

Figure 3.6: Solid curves: Conventional polarimeter measurements of polarization rotation in the presence of milk (2% homogenized cow's milk, Kroger Dairy). Dashed curves: Rotating polarization polarimeter measured polarization rotation by water, fructose, and glucose solutions in the presence of larger quantities of milk. The light grey area represents the regime where the conventional polarimeter fails to accurately measure the polarization rotation, and the dark grey area represents the regime where rotating polarization polarimeter fails.

Next, we used 2% homogenized cow's milk as a source of DLS. Milk is a natural substance that exhibits considerable amount of scattering (responsible for milk's opaque white appearance). Milk also mixes homogeneously with water solutions of fructose and glucose. Fig. 3.6 shows a comparison between the response of the RP polarimeter (dashed curves) with that of a conventional polarimeter (solid curves) in measuring the polarization rotation caused by water and solutions of glucose (1M)

and fructose (1M) in the presence of increasing amounts of milk. Note that the conventional polarimeter fails to determine the polarization rotation in the presence of 5% milk or more, whereas the RP polarimeter accurately detects the polarization rotation in the presence of up to 20% milk.

3.5 Discussion

Fig. 3.7 provides a clearer picture of the RP polarimeter's immunity to significant DLS. While the lock-in phase determines the polarization rotation, the lock-in amplitude is a measure of the fraction of unscattered light (eq. 3.19). So in Fig. 3.7, we examine the normalized lock-in amplitude vs. milk concentration (solid line). For comparison, we also show the calculated fraction of unscattered light estimated by the Beer-Lambert's Law (dashed line) i.e. an exponential decrease of the intensity of unscattered light with distance and scatterer concentration.

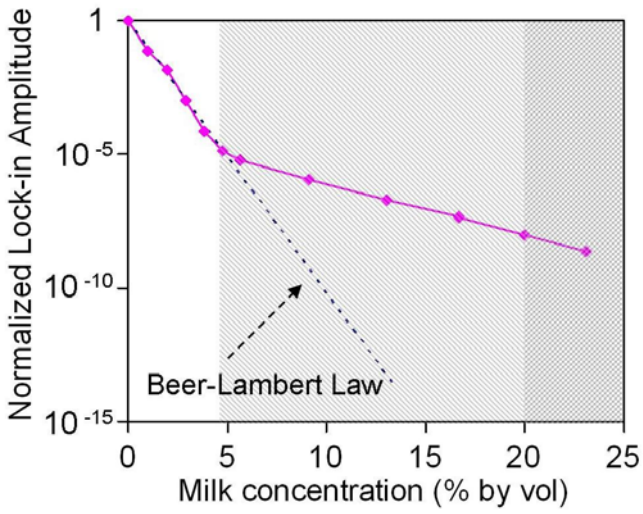

Figure 3.7: Solid curve: Normalized lock-in amplitude as measured by the RP Polarimeter vs. milk concentration. Dashed curve: Estimated fraction of unscattered light (from Beer-Lambert's Law). The light grey area represents the regime where the conventional polarimeter fails to accurately measure the polarization rotation and the dark grey area represents the regime where the rotating polarization polarimeter fails.

The 4-fold increase in the concentration of milk (from 5% to 20%) corresponds to three orders of magnitude decrease in the fraction of unscattered light. Note that the actual fraction of photons that remained unscattered at larger milk concentrations were measurable, and thus, greater than the estimation from Beer-Lambert's Law (it is known that Beer-Lambert's Law breaks down for large concentrations of scatterers [53]). This polarimeter significantly outperforms conventional polarimeters in the presence of three orders of magnitude more DLS.

The use of a lock-in detector to extract the phase of a signal component at any reference frequency (here 4ω) provides a significant dynamic range (over 9 orders of magnitude change in the signal amplitude in our setup) for measurement. The sensitivity and accuracy of the detector in measuring the phase remains roughly constant throughout this range, and these numbers deteriorate only when the amplitude of the desired signal component at the reference frequency is reduced to less than 10^{-6} of the total signal. The sources of noise are the unwanted forward scattered signal, rotational frequency instability of the motor, and the inherent noise in the electrical components of the setup.

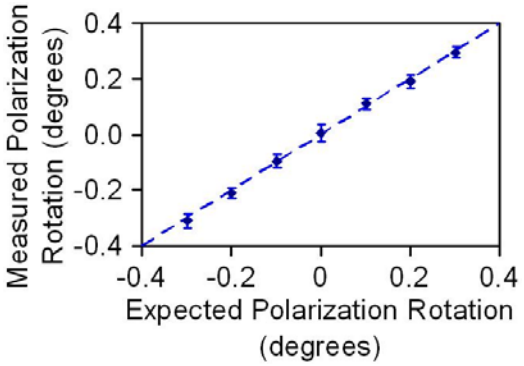

Figure 3.8: The RP polarimeter measures a variation in polarization rotation smaller than 0.1° in the presence of 15% milk (2% homogenized cow's milk, Kroger Dairy), with standard deviations up to ± 0.035°.

Our RP polarimeter can measure a variation of less than 0.1° of polarization rotation in the presence of more than 15% milk (by volume), with standard deviations in the measurement of the phase values of up to ± 0.035° (Fig. 3.8). For glucose sensing applications, the sensitivity of our device is ~ 20g/ℓ ± 7g/ℓ for a 1 cm long path length sample cell. Thus, this polarimeter is not sensitive enough to measure typical blood glucose values in humans. Its sensitivity could be increased further by improving the mechanical stability of the motor and the QWP/mirror attached to it, thus achieving a more stable mechanical rotation frequency.

We note that some constituents of milk are also chiral in nature, mostly lactose, which constitutes ~5% of milk (~12 g per 240 mℓ) [54]. Since the specific rotation of lactose is 55°/(g/mℓ)/dm, we expect 100% milk to rotate the polarization of linearly polarized light in a 1 cm long sample cell by 0.275°. The maximum concentration of milk in our solutions was 25%, which means that the contribution of milk in the total polarization rotation was always below 0.07°. We were unable to see the small contribution of milk to overall polarization rotation in our experiments due to insufficient sensitivity in our current setup.

CHAPTER 4: DEVELOPING A HARMONIC GENERATION POLARIMETER

4.1 Introduction

Optically precise polarization measurements, comprising the basis for methods of high sensitive polarimetry and polarization spectroscopy, are generally employed in a host of experiments for the measurement of limiting small quantities. These methods, as a rule, are based on the use of polarized light with a high degree of linear polarization, which, in many cases, determines the limiting sensitivity of the polarization measurements [55]. The degree of linear polarization is defined as the ratio of light intensity components polarized orthogonal to the desired polarization to the light intensity component with desired polarization.

The degree of polarization is estimated from the *extinction ratio* (**ER**) of a polarizer pair (polarizer - analyzer), the measure of effectiveness of the polarizers in separating the orthogonal polarization components of input light. ER is the ratio of light transmitted when the polarizers are crossed (transmission minimum) to that when they are parallel (transmission maximum). ER depends on the quality of both polarizer and analyzer, and the quality of the analyzer must clearly not be inferior to that of the polarizer. All polarizers vary in effectiveness of their separation of the polarization components, and may be called *leaky* or partial polarizers.

Polarizers utilize one or both of two polarization dependent optical phenomena: *dichroism* -- selective absorption of one of the two orthogonal polarization components of an input beam; and *birefringence* – two different indices of refraction for two orthogonal polarization components, causing the two orthogonal polarization components of the input light to follow different paths and separate.

Wire-grid polarizers exhibit dichroism, however, are not in use because they are difficult to manufacture. Dichroic mineral crystals like tourmaline, hypersthene exhibit strongly wavelength dependent absorption, and hence have limited application [56]. In 1928 Edwin Herbert Land invented the first dichroic sheet polarizer, known as the Polaroid J-sheet. The most widely used linear polarizer is the Polaroid H-sheet, which is a molecular analogue of the wire-grid polarizers [56]. The H-sheet is a very effective polarizer across the entire visible spectrum, and the molecular dimension of the dichromophores (each miniscule dichroic entity) ensures that scattering represents no problem. Polaroid sheets are suitable for low intensity applications, and their ER range from 10^{-2} to 10^{-4} [57, 58].

Naturally occurring calcite crystal is the most popular material used for manufacturing birefringent polarizers. Its very high optical quality allows obtaining light with a high degree of linear polarization. Typical ER for calcite *Glan-Laser* (**GL**) air spaced polarizers are from 10^{-4} to 10^{-6}, depending on the crystal quality [59]. To achieve a better ER with calcite polarizers, one has to follow these instructions [60, 61]: 1- select a pair of the best quality polarizers; 2- choose the beam direction in the polarizer and analyzer; 3- use a small diameter beam; 4- select the best place at the prism surface; 5- increase the distance between the analyzer and the photo-receiver; 6- use diaphragms to block scattered ordinary rays.

Another way to obtain a lower ER is to use *nonlinear optical* (**NLO**) crystals as polarizers. Nonlinear optical processes such as *second harmonic generation* (**SHG**) and *sum frequency generation* (**SFG**) that are used in optical frequency conversion techniques are highly polarization dependent. Therefore, NLO crystals can be used as sources of high-degree polarized light and as analyzers of polarized laser beams. In 1987 Zheludev et. al. first demonstrated the use of a SHG NLO crystal (KDP,

CDA) as a polarizer [62]. Among crystals of water-soluble group of KDP, the best ER ($5x10^{-9}$) was obtained from KD*P crystal based polarimeter that had a SHG crystal as polarizer and a SFG crystal as analyzer [63, 64]. The large selection of NLO crystals applicable in the UV, visible, and especially the IR spectral region along with the use of ultrashort pulses enables the development of these crystals as polarizers and analyzers.

We examine the polarizing and analyzing potential of *beta - Barium Borate* (**β-BaB_2O_4**, known as **BBO**) with ultrashort pulse light sources. BBO is a widely used negative-uniaxial NLO crystal because of its wide transparency and phase matching ranges, large nonlinear coefficient, high damage threshold and excellent optical homogeneity. BBO Crystal is of particular importance in the visible and UV, for it can be used for SHG to wavelengths as short as 204.8 nm and SFG to even shorter wavelengths (193nm) [65]. Further, we also investigate different NLO crystal based polarimeter schemes to work with ultrashort pulsed light sources.

4.2 Methods and Instruments

4.2.1 SHG crystal as a Source of Polarized Light

For phasematched conversion of optical frequencies in a NLO crystal, the waves at the converted frequency are polarized with a definite form. As an example, for negative uniaxial crystals (such as BBO, KDP), two types of phasematched SHG processes are possible: Type-I - two *ordinary* (**O**) incident waves produce an *extraordinary* (**E**) *second harmonic* (**SH**) wave, denoted as OOE process; Type-II - one ordinary and one extraordinary fundamental waves produce an extraordinary SH wave, denoted as OEE process. According to the nature of these processes, the polarization of the resulting extraordinary wave has to be ideal. Thus, the SHG crystal becomes a source of highly-polarized light.

Nevertheless, there are some effects that reduce polarization purity of the output SH wave: depolarization due to volume inhomogeniety in the crystal, quality of crystal output surface, gain induced and thermally induced voltages due to the absorption of light, and optical activity [63]. These factors affect conventional polarizers and other optical elements to the same extent, and are not considered in detail.

Another major reason influencing the degree of polarization of the output SH beam is the generation of SH O- and E-wave as a result of the non-phasematched processes in the crystal. For negative uniaxial crystals, they are OOO, OEO, EEO and EEE. Some of these processes can be forbidden because of crystal symmetry and orientation. Fig. 4.1 shows a typical setup used to determine the polarization purity of the SH from Type-I BBO crystal, with a 800nm center wavelength source.

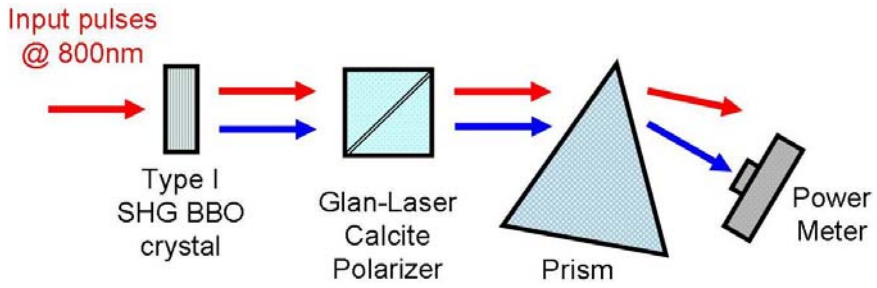

Figure 4.1: Type-I SHG BBO - calcite polarizer setup.

4.2.2 SHG / SFG Crystal as an Analyzer of Polarized Light

SHG crystals can also be used for the analysis of the state of polarization of the converted light, as the conversion efficiency for the SHG process depends on the state of the polarization of the incident light. SFG crystals can also fill the role of a polarization analyzer by the summation of *probe* and *pump* waves, wherein the state of polarization of the probe wave is

determined by the intensity of light at the summed frequency, and the pump wave is used to obtain the required efficiency of frequency conversion.

There are three main reasons limiting the ER of a SHG / SFG crystal analyzer: polarization impurity of the input beam(s); depolarization of the input beam(s) on the crystal face and inside its volume; non-phasematched processes. The former two reasons lead to generation of undesired phasematched signal. Choice of a NLO crystal with certain crystal symmetry, and appropriate orientation of the crystal can eliminate many non-phasematched processes. ER will then be limited only by the polarization purity of the fundamental beam and its further depolarization by the crystal, and thus minimized. Fig. 4.2 shows a typical setup used to determine the analyzing prowess of the SHG BBO crystal, with a 800nm center wavelength source.

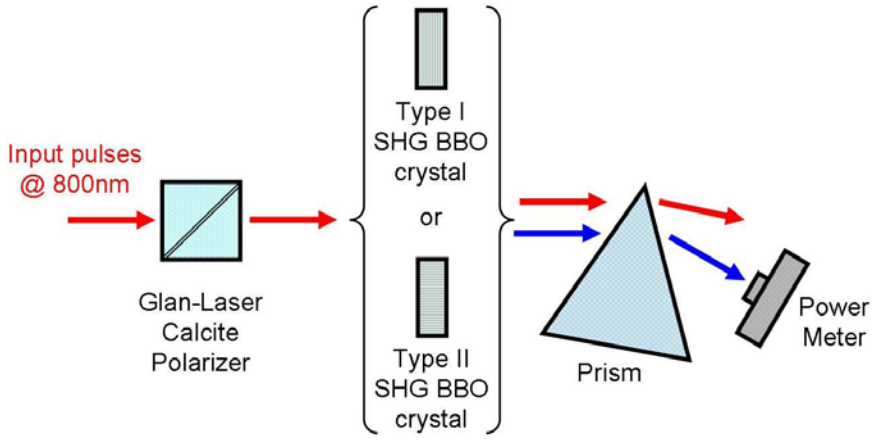

Figure 4.2: Type-I or II SHG BBO crystal analyzer setup.

4.2.3 Design of a Collinear Nonlinear Crystal based Polarimeter

As mentioned earlier, SHG crystals can provide light with higher degree of polarization as compared to calcite polarizers. Also, since the quality of the analyzer should be no less than the polarizer to achieve the best ER, a SHG / SFG crystal was used as an analyzer of the state of polarization of the light from the SHG crystal. We considered various schemes for the design of a collinear NLO crystal based polarimeter to be used with ultrashort pulsed light sources, utilizing a combination of SHG (BBO / KDP) crystal polarizers and SHG / SFG (BBO) crystal analyzers. Table 4.1 shows the convention used in depicting the intensities and polarization of the beams in the following polarimeter schemes. The color is associated to the wavelength of the beams $(\lambda_{RED} > \lambda_{BLUE} > \lambda_{VIOLET})$.

Table 4.1: Convention used in the following polarimeter schemes to depict the intensity and polarization of individual beams.

⟶	Strong intensity
⇢	Weak intensity
O	O polarization
|	E Polarization

In the SHG - SHG scheme (Fig. 4.3), a Type-I SHG crystal polarizer creates a polarized SH (blue) beam with high degree of polarization from the lesser polarized fundamental (red) input beam. The state of polarization of the blue beam is analyzed with another SHG crystal, which creates an output (violet) beam as the *fourth harmonic* (**4H**) of the fundamental frequency (red).

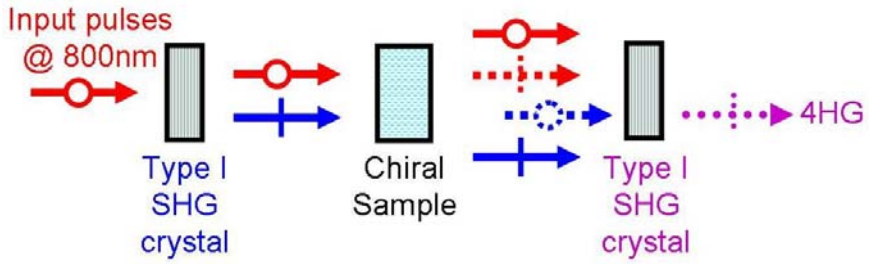

Figure 4.3: Proposed SHG - SHG scheme.

The low intensity of the 4H violet beam at the analyzer because of the compounding effect of low efficiency conversions at the two stages will require very sensitive detectors for measurement. There will be a non-phasematched 4H signal generated from the red beam in the analyzer crystal, so it is necessary to remove the red beam after the polarizer crystal. There will also be a non-phasematched SHG from the blue beam in the analyzer crystal. Upon suppressing all the undesired non-phasematched processes, the output 4H intensity becomes proportional to the square of the intensity of the blue O beam, and ER becomes largely a function of the polarization purity of blue beam.

In the SHG - SFG (Type-I) scheme (Fig. 4.4), a Type-I SHG crystal polarizer creates a polarized SH (blue) beam with high degree of polarization from the lesser polarized fundamental (red) input beam. The state of polarization of the blue beam is analyzed with a SFG (Type-I) crystal, which creates an output (indigo) beam as the *third harmonic* (**3H**) of the fundamental frequency (red).

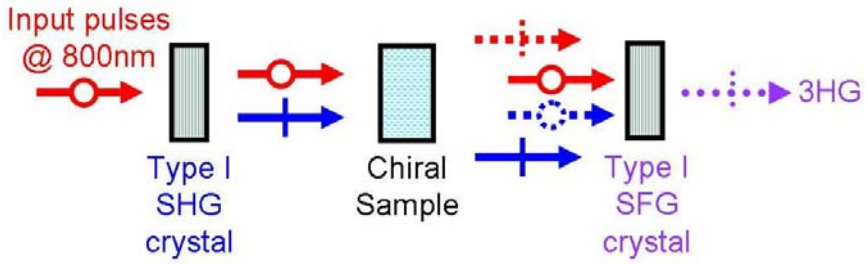

Figure 4.4: Proposed SHG - SFG (Type-I) scheme.

The intensity of the 3H indigo beam at the analyzer is less weak compared to the 4H signal in the SHG - SHG scheme, because of the strong fundamental red O beam with a weak blue O beam in the phasematched process. The intensity of 3H is linearly dependent on the polarization state of the blue beam, and the ER depends on the polarization purity of the highly polarized blue beam. An advantage of this scheme is the ability to spectrally filter the light generated from all NLO processes due to the individual beams, since they will result in outputs at different frequencies.

There is also some 3H obtained through the non-phasematched Type-I SFG from the weak red E beam and strong blue E beam in the analyzer crystal. It may be possible to phasematch for this process instead, however, it reduces the ER because the ER now depends on the polarization purity of the lesser polarized red beam. 3H obtained from the strong red O beam and the strong blue E beam through non-phasematched SFG Type-II process is also a background.

In the SHG - SFG (Type-II) scheme (Fig. 4.5), a Type-I SHG crystal polarizer creates a polarized SH (blue) beam with high degree of polarization from the lesser polarized fundamental (red) input beam. The state of polarization of the blue beam is analyzed with a SFG (Type-II)

crystal, which creates an output (indigo) beam as the third harmonic (3H) of the fundamental frequency (red).

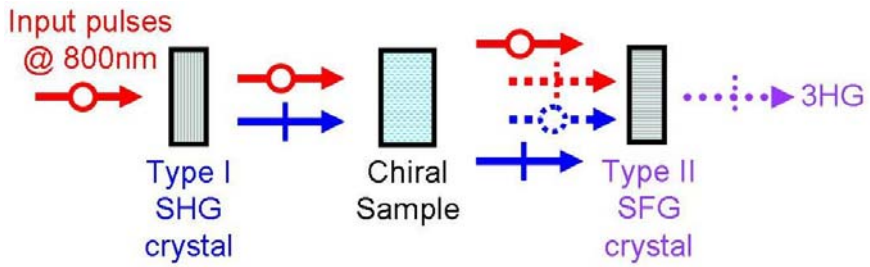

Figure 4.5: Proposed SHG - SFG (Type-II) scheme.

The intensity of the 3H indigo beam at the analyzer is weaker compared to the 3H signal in the SHG – SFG (Type-I) scheme, because of the weak fundamental red E beam with a weak blue O beam in the phasematched process. The intensity of 3H is dependent on the polarization state of both the blue and the red beam, and the ER depends on the polarization purity of both the beams. The advantageous ability to spectrally filter out all NLO processes due to the individual beams remains the same as in the SHG - SFG (Type-I) scheme.

There is also a 3H signal obtained through the non-phasematched Type-II SFG from the strong red O beam and strong blue E beam in the analyzer crystal. It may be possible to phasematch for this process instead; however, it suffers from the same disadvantages as the previous Type-II process. 3H obtained from other non-phase matched processes such as SFG Type-I will also be a background.

4.3 Theory

The ER of a NLO crystal optimized for a particular phasematched second-order nonlinear optical process is the ratio of generation minimum (for input polarization orthogonal to the phasematching polarization) to generation maximum (for phasematching input polarization) of the desired frequency output. The best possible ER derived solely from second-order nonlinear processes requires elimination or suppression of the non-phasematched processes, while simultaneously enhancing the phasematched process.

4.3.1 Second-Order Nonlinear Optical Processes

Several nonlinear optical effects are associated with the second-order susceptibility tensor $\chi^{(2)}$: *second harmonic generation* (**SHG**, volume and surface); *sum frequency generation* (**SFG**); *difference frequency generation* (**DFG**); *optical parametric amplification* (**OPA**); *optical parametric oscillation* (**OPO**); *optical rectification* (**OR**); and three-wave mixing (encompasses many of the previously mentioned processes).

To understand the origin of different $\chi^{(2)}$ processes, consider an optical field incident upon a nonlinear optical medium that consists of two distinct frequency components.

$$\tilde{E}(t) = E_1 e^{-i\omega_1 t} + E_2 e^{-i\omega_2 t} + \text{c.c.} \qquad [4.1]$$

The induced nonlinear polarization is described by expressing it as a power series in the field strength $\tilde{E}(t)$ [66].

$$\begin{aligned}\tilde{P}(t) &= \chi^{(1)}\tilde{E}(t) + \chi^{(2)}\tilde{E}(t)^2 + \chi^{(3)}\tilde{E}(t)^3 + \ldots \\ &\equiv \tilde{P}^{(1)}(t) + \tilde{P}^{(2)}(t) + \tilde{P}^{(3)}(t) + \ldots\end{aligned} \qquad [4.2]$$

The second-order nonlinear polarization $\tilde{P}^{(2)}(t)$ is given by

$$\tilde{P}^{(2)}(t) = \chi^{(2)}\tilde{E}(t)^2$$

$$\begin{aligned}\tilde{P}^{(2)}(t) = {} & \chi^{(2)}E_1^2 e^{-2i\omega_1 t} && \text{(SHG from } \omega_1\text{)} \\ & + \chi^{(2)}E_2^2 e^{-2i\omega_2 t} && \text{(SHG from } \omega_2\text{)} \\ & + 2\chi^{(2)}E_1E_2 e^{-2i(\omega_1+\omega_2)t} && \text{(SFG from } \omega_1 \text{ and } \omega_2\text{)} \\ & + 2\chi^{(2)}E_1E_2^* e^{-2i(\omega_1-\omega_2)t} && \text{(DFG from } \omega_1 \text{ and } \omega_2\text{)} \\ & + 2\chi^{(2)}\left[E_1E_1^* + E_2E_2^*\right] && \text{(OR)}\end{aligned} \qquad [4.3]$$

In Eq. 4.3, we have not shown the complex conjugates of the terms, which result in a response at the negative of each of the non-zero frequencies. Typically no more than one non-zero frequency component of the resultant $\tilde{P}^{(2)}(t)$ will have an appreciable intensity, because the generated intensity from a particular nonlinear process depends on certain phasematching conditions that usually cannot be satisfied for multiple processes simultaneously. However the light intensity resulting from undesired processes contributes towards the ER of a NLO crystal.

Following rules are generally practiced to achieve efficient frequency conversion [67]: A NLO crystal with minimal absorption at the interacting wavelengths is chosen, with sufficiently large $\chi^{(2)}$, and allows phasematching; the particular phasematching direction with the

appropriate polarizations for the interactive waves is selected to optimize the effective nonlinear susceptibility, d_{eff}; the length of the crystal is finally chosen to achieve the desired conversion efficiency.

$$d_{eff} = \frac{1}{2}\chi^{(2)}_{eff} = \hat{e}_3 \cdot d \cdot \hat{e}_1\ \hat{e}_2 \qquad [4.4]$$

where $\hat{e}_1$, $\hat{e}_2$ and $\hat{e}_3$ are the respective E-field polarizations of the three interacting waves, and d represents the d-Matrix of the NLO crystal.

The interacting E-fields (at input, and generated frequencies) are composed of orthogonally polarized components - *ordinary* (**O**) and *extraordinary* (**E**) - based upon propagation inside the nonlinear crystal. Second-order NLO processes are categorized on the basis of polarizations of the interacting E-fields, such as OOO, OOE, OEO, OEE, EOO, EOE, EEO, and EEE process, where the letters describe the polarization of the interacting beams. These processes are further categorized as: Type-I, when the polarizations of the two pump beams are the same and orthogonal to the polarization of signal beam (OOE, EEO); and Type-II, when the polarizations of the two pump beams are orthogonal to each other and the polarization of the signal beam is the same as one of the pump beams (OEO, OEE, EOO, EOE).

4.3.2 Nonlinear Crystals

NLO crystals belong to one of many crystal point groups. The nonlinear coefficient d-matrix, used in second-order nonlinear optics, has a unique form for each crystal point group. Symmetry conditions simplify the d-matrix, where most of the elements either become zero or equal to ± 1 times other elements [66, 68]. The choice of a polarizing and/or analyzing nonlinear crystal, apart from transparency and phasematching constraints,

also depends on the symmetry conditions and nonlinear coefficients of a crystal that may inhibit the undesired and/or enhance the desired NLO process. For example, OOO process is forbidden for any orientation of crystals belonging to point group $\bar{4}2m$ (such as KDP)[69].

In our NLO crystal polarimeter schemes, BBO was a crystal of choice for its excellent transmission range and phasematching ability for desired SHG / SFG interaction and conversion wavelengths (for 800nm source (800nm, 400nm, 266.7nm) and for 1030nm source (1030nm, 515nm, 343.3nm)), large nonlinear coefficients that help achieve high conversion efficiency for shorter length of crystals (for comparison, ~1/6 as needed for KDP), high damage threshold for use with intense ultrashort pulses, and excellent optical homogeneity that reduces polarization deterioration of the beams.

4.3.3 SHG / SFG Conversion Efficiency

The conversion efficiency of SHG and SFG (in the infinite plane-wave, negligible pump depletion approximations) are given by [68]

$$\eta_{2\omega} = \frac{8\pi^2 d_{eff}^2 L^2 I_\omega}{\varepsilon_0 n_\omega^2 n_{2\omega} c \lambda_\omega^2} \cdot \mathrm{sinc}^2\left(\Delta kL/2\right) \qquad [4.5]$$

$$\eta_{\omega_1+\omega_2} = \frac{8\pi^2 d_{eff}^2 L^2 I_{\omega_1}}{\varepsilon_0 n_{\omega_1} n_{\omega_2} n_{\omega_3} c \lambda_{\omega_1+\omega_2}^2} \cdot \mathrm{sinc}^2\left(\Delta kL/2\right) \qquad [4.6]$$

where d_{eff} is the effective nonlinear coefficient, L is the length of the crystal, I_ω is the intensity at frequency ω, Δk is the phase velocity mismatch, n_ω is the index of refraction at ω, and λ_ω is the wavelength corresponding to ω. Under perfect phasematching conditions, the

conversion efficiency can become appreciable, which results in depletion of the pump beam intensity. The expressions for conversion efficiency of perfectly phasematched SHG and SFG (infinite plane-wave approximation) while accounting for pump depletion are [68]

$$\eta_{2\omega} = \tanh^2\left(\sqrt{\frac{8\pi^2 d_{eff}^2 L^2 I_\omega(0)}{\varepsilon_0 n_\omega^2 n_{2\omega} c \lambda_\omega^2}}\right) \qquad [4.7]$$

$$\eta_{\omega_1+\omega_2} = \frac{\lambda_{\omega_2}}{\lambda_{\omega_1+\omega_2}} \begin{cases} \sin^2\left(\sqrt{\dfrac{8\pi^2 d_{eff}^2 L^2 I_{\omega_1}(0)}{\varepsilon_0 n_{\omega_1} n_{\omega_2} n_{\omega_3} c \lambda_{\omega_2} \lambda_{\omega_1+\omega_2}}}\right) & , \left|\sqrt{\dfrac{\lambda_{\omega_2} I_{\omega_2}(0)}{\lambda_{\omega_1} I_{\omega_1}(0)}}\right| \ll 1 \\ \tanh^2\left(\sqrt{\dfrac{8\pi^2 d_{eff}^2 L^2 I_{\omega_1}(0)}{\varepsilon_0 n_{\omega_1} n_{\omega_2} n_{\omega_3} c \lambda_{\omega_2} \lambda_{\omega_1+\omega_2}}}\right) & , \left|\sqrt{\dfrac{\lambda_{\omega_2} I_{\omega_2}(0)}{\lambda_{\omega_1} I_{\omega_1}(0)}}\right| = 1 \end{cases} \qquad [4.8]$$

4.3.4 Effect of Crystal Orientation

The orientation of a NLO crystal is parameterized with two angles: θ represents the angle between the beam propagation vector and the crystalline z-axis (optic axis); φ represents the azimuthal angle between the propagation vector and the *xz*-crystalline plane.

The phase mismatch ΔkL for NLO processes is a function of θ, and the crystal is tuned to the critical phasematching angle θ_{PM} for achieving maximum conversion efficiency. The phase mismatch for SHG and SFG processes are calculated as

$$\Delta k_{SHG} L = \left(2k_\omega - k_{2\omega}\right)L; \qquad \Delta k_{SFG} L = \left(k_{\omega_1} + k_{\omega_2} - k_{\omega_1+\omega_2}\right)L \qquad [4.9]$$

where $k_\omega = n_\omega(\theta)\omega/c$, L is the length of the crystal, $n_\omega(\theta)$ is the index of refraction experienced by a given polarization (O or E) component of light at frequency ω for the crystal orientation angle θ.

The dependence of phase mismatch on ω implies that different NLO SHG / SFG process (such as OOE, OEE, etc) achieve phasematching at different frequencies for a given crystal orientation θ. In other words, to obtain light at a desired frequency from pump beams at specific input frequencies, only one NLO process can be phasematched at its phasematching angle θ_{PM}, all other NLO processes are suppressed (Fig. 4.6). Note that the spectral contribution from the phasematched NLO process for correct input polarization (O for the OOE process in Fig. 4.6) is orders of magnitude larger at the desired conversion frequency.

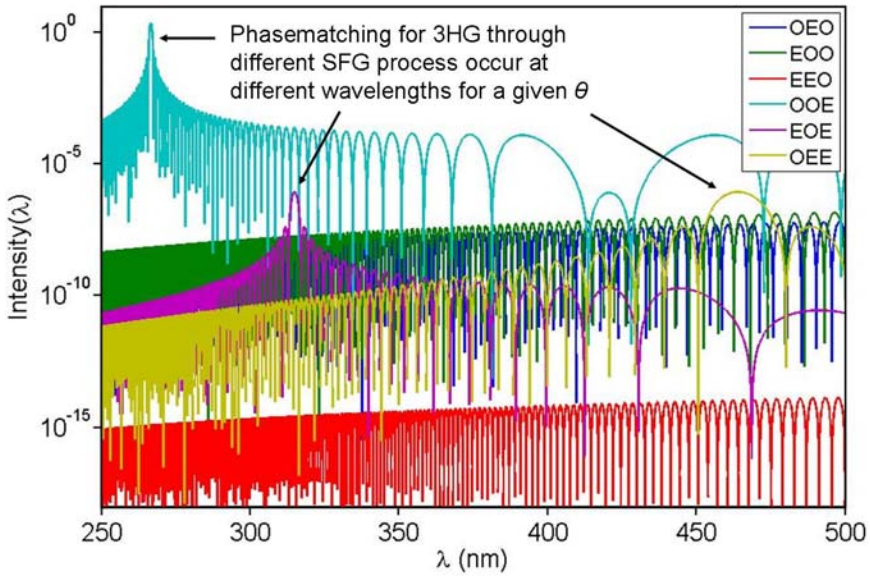

Figure 4.6: Simulated spectral variation of the output 3HG through SFG of fundamental and SH beams for different processes to show the effect of ΔkL. Simulation assumes a BBO crystal oriented at $\theta = 44.3^\circ$ (phasematching angle for OOE process to obtain output at 3H of 800nm), and the polarization of both the fundamental and SH pump beams to be O with a polarization purity of 10^{-3}.

The effective nonlinear coefficient d_{eff} is usually a function of both θ and φ [66, 68]. While θ is usually set to θ_{PM} for the desired phasematched NLO process, φ is usually set to maximize d_{eff} for the phasematched NLO process. To achieve the best ER while maintaining good conversion efficiency, an optimized set (θ,φ) along with the most appropriate NLO process to be used with a NLO crystal is derived from simulation.

4.3.5 Effect of Crystal Length

The length of the NLO crystal set at (θ,φ) further establishes the conversion efficiency for all the second-order processes. Long crystals are routinely used to achieve high conversion efficiencies. The use of longer crystals, however, also increases the phase mismatch for a NLO process for a given orientation angle θ. This results in reduction of the range of wavelengths that are effectively phasematched in that NLO process (a quantity known as the *phasematching bandwidth*). As an example, the phasematching bandwidth $\delta\lambda_{SHG}$ of a SHG process for pump beam with center wavelength λ_0, and a crystal of length L is [70, 71]

$$\delta\lambda_{SHG} = \frac{0.44\,\lambda_0/L}{\left|n'(\lambda_0) - \frac{1}{2}n'(\lambda_0/2)\right|} \qquad [4.10]$$

where $n'(\lambda_0)$ is the value of $dn/d\lambda$ at λ_0. While this effect poses negligible problems for frequency conversions from narrow-band pulses, ultrashort pulses that are usually fairly broadband show $sinc^2$ oscillations in the spectrum.

.

4.4 Results

The polarization purity of our laser sources were measured using different uncoated GL polarizers, and were found to be ~10^{-2}. Table 4.2 shows the polarization measurements done on the output pulses from Amplitude Systemes t-Pulse 500 (450fs, 1030nm center wavelength, 400nJ per pulse).

Table 4.2: Measured polarization putrity of t-Pulse 500 output pulses (450fs, 1030nm center wavelength, 3nm bandwidth) tested by different polarizers

Polarizer	Achieved Extinction Ratio
Newport 10GL08	1.37×10^{-2}
Karl Lambrecht MGLQD08 (1)	1.64×10^{-2}
Karl Lambrecht MGLQD08 (2)	1.32×10^{-2}

The ability of a GL polarizer to increase the polarization purity of the source (t-Pulse 500) was tested by setting a GL polarizer (Karl Lambrecht MGLQD08) after the laser, and analyzed with other GL polarizers (Table 4.3).

Table 4.3: Measured polarization purity of t-Pulse 500 output pulses (450fs, 1030nm center wavelength, 400nJ per pulse) tested by different GL polarizers

Analyzer	Achieved Extinction Ratio
Newport 10GL08	1.32×10^{-6}
Karl Lambrecht MGLQD08 (1)	9.61×10^{-7}

Since the dynamic range of power detectors is limited, measurements are done around the transmission minima of the analyzer. Curve-fitting the measurements to modified Malus law (eq. 4.11) extracts the maximum and minimum transmission intensities from the plot of Transmission Power vs. Analyzer angle, which are then used to calculate the ER (= P_{min} / P_{max}) (see Fig. 4.7).

$$P_{transmitted} = (P_{max} - P_{min}) \sin^2(\theta) + P_{min} \qquad [4.11]$$

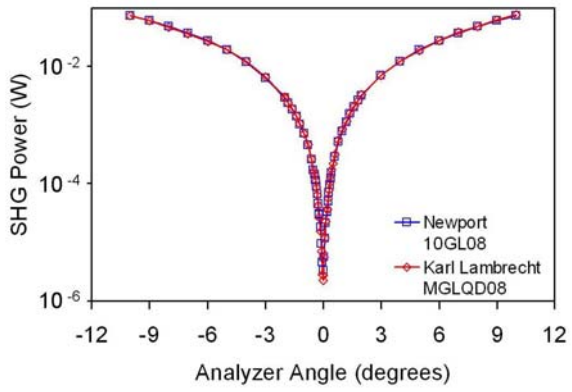

Figure 4.7: Measured transmitted power vs Analyzer angle for two GL polarizers for a laser source (t-Pulse 500) polarized by a GL Polarizer (Karl Lambrecht MGLQD08). Typical ER was measured to better than 10^{-6}.

Different NLO crystals (material and size) were used to create SHG from t-Pulse 500. The polarization purity of the SH was measured using a GL polarizer (Fig. 4.8). The best ER of 8.71 x 10^{-5} was obtained for a thick (3.5mm) BBO crystal.

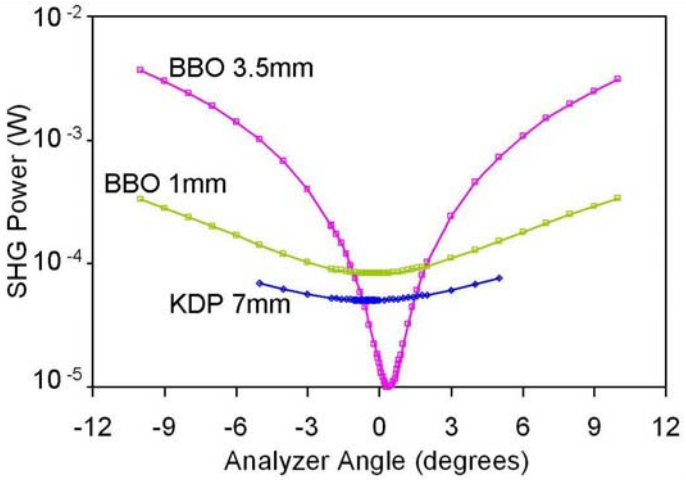

Figure 4.8: Measured transmission power vs. Analyzer angle for SH of t-Pulse 500 for different crystals. The best polarization purity was found for 3.5mm BBO.

The capacity of different NLO crystals to analyze the state of polarization is measured by changing the rotation of the input light beam polarization (Table 4.4, Fig. 4.9). Thicker crystals are observed to provide better ER as expected from tighter phasematching conditions.

Table 4.4: Measured ER for different crystals used as Analyzer for KM Labs oscillator output pulses (100fs, 800nm center wavelength, 2nJ per pulse)

SHG Crystal	Crystal Length (mm)	Achieved Extinction Ratio
BBO	0.5	1.05×10^{-5}
BBO	3.5	7.65×10^{-6}
$LiIO_4$	1	8.18×10^{-5}
$LiIO_4$	10	6.65×10^{-6}
$LiIO_4$	20	8.94×10^{-6}

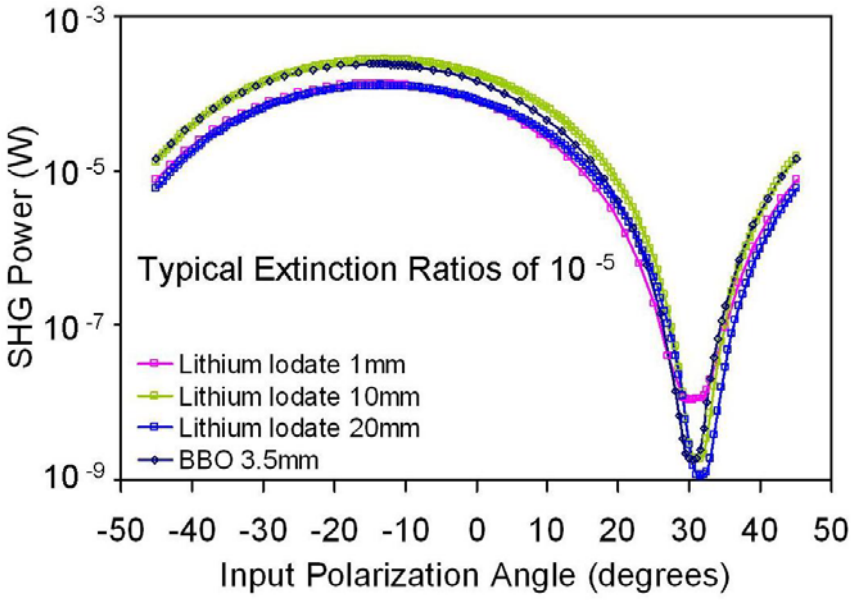

Figure 4.9: Measured SHG output power vs input polarization angle for different NLO crystals. The best ER was obtained for 10mm $LiIO_4$ crystal. A KM Labs oscillator was used as source (100fs, 800nm center wavelength, 2nJ per pulse).

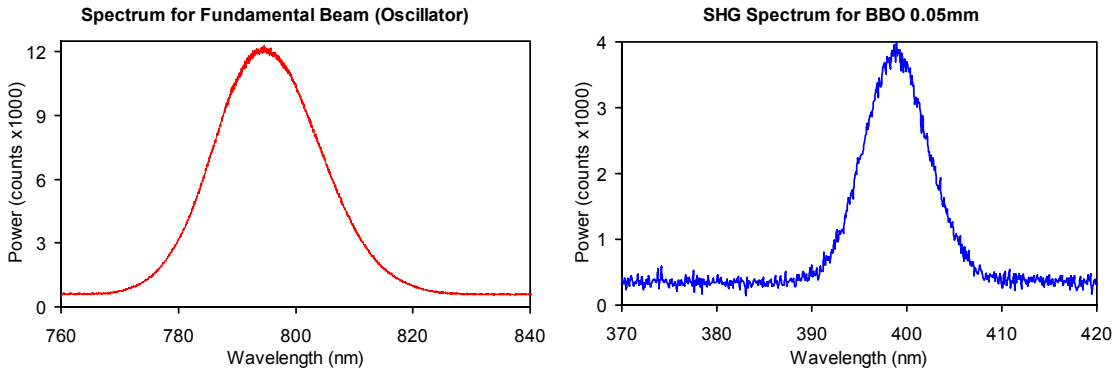

Figure 4.10: (Left) Measured spectrum of the input pulse derived from KM Labs oscillator (100fs, 800nm center wavelength, 2nJ per pulse). (Right) Measured SHG spectrum for a 0.05mm BBO crystal for which the entire bandwidth of the input pulses is phasematched.

Separately, the decrease in phasematching bandwidth for thicker crystals was verified using different sizes of BBO crystal and Type-I SHG. The output SHG spectrum shows $sinc^2$ oscillations when phasematching

bandwidth becomes comparable to or smaller than the bandwidth of fundamental pulses (Fig. 4.10, 4.11, 4.12).

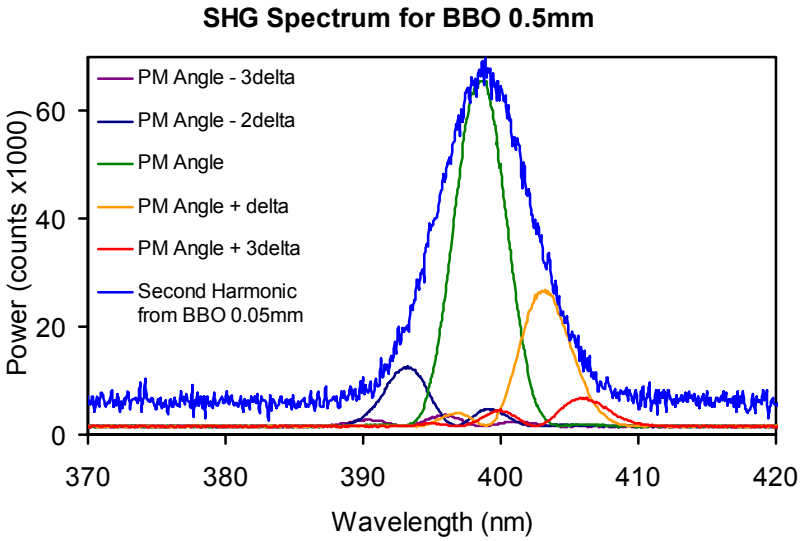

Figure 4.11: Measured SHG spectrum for a 0.5mm BBO crystal with a smaller phasematching bandwidth shows $sinc^2$ oscillations. Tuning the crystal phasematching angle θ by small amounts δ shifts the center wavelength of frequency conversion process. The SHG intensity is the highest when phasematching the center wavelength of the input pulse.

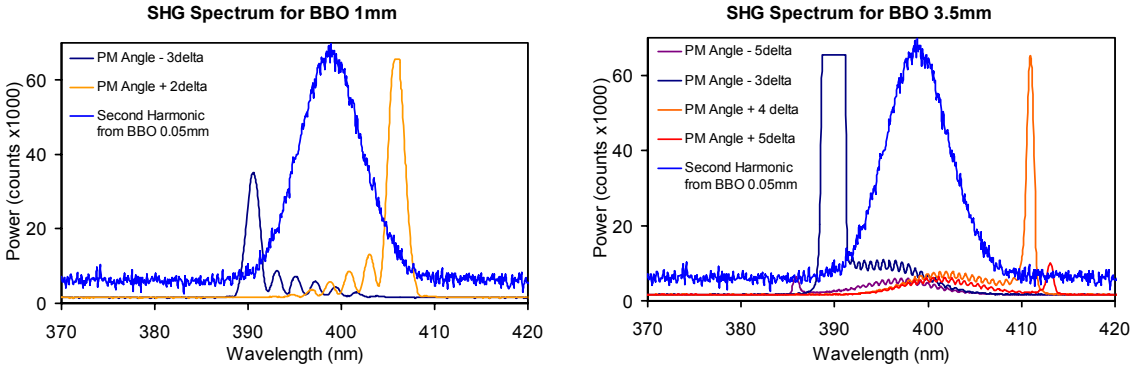

Figure 4.12: Measured SHG spectrum for 1mm and 3.5mm BBO crystals. The $sinc^2$ oscillations become faster for thicker crystals. The crystal phasematching angle θ is tuned by small amounts δ to see the shift in the center wavelength of frequency conversion process.

4.5 Discussion

The ultrashort pulses from the aforementioned lasers sources were found to have poor degrees of linear polarization, 10^{-2} at best. However, we observed an ER of 10^{-6} using the best GL polarizers available to us (Karl Lambrecht MGLQD08).

The polarizing powers of the SHG crystals were examined by determining the degrees of linear polarization of the SH produced by crystals. The SH obtained from different crystals (materials and sizes) has a higher degree of linear polarization as compared to that of the input laser pulses as expected (up to 3 orders of magnitude). The input pulses were polarized by a GL polarizer to enhance the polarization purity of the input pulses to further enhance the polarization purity of the SH.

The SH obtained in the lab from various crystals, however, still lacks the expected polarization purity of better than the GL polarizers. This is mainly attributed to the surface inhomogeniety in the crystal (causing depolarization), and also non-optimal crystal thickness (causing insufficient filtering of unwanted NLO processes).

The analyzing powers of the SHG crystals were examined by determining the degree of linear polarization of the laser pulses polarized by a GL polarizer. The ER obtained from different crystals (materials and sizes) matched the ER obtained from another GL polarizer (10^{-6}). This establishes NLO crystals as excellent analyzers of polarized light. Since the analyzed light has a degree of linear polarization only as good as 10^{-6} to begin with (polarizing power of a GL polarizer), NLO crystals are expected to provide even higher ER with a purer polarized light.

CHAPTER 5: CONCLUSIONS AND FUTURE DIRECTION

5.1 Oscillating Polarization Scheme

As all chiral molecules display optical rotation (they rotate the polarization of light, a property that is also called “optical activity”), polarimetry would seem to be an excellent technique for search and optimization of enantioselective compounds and processes. A multi-parameter measurement polarimetry technique would be much more useful for unique identification of chiral species. So, I attempted to develop a powerful polarimetry apparatus suitable for the simultaneous measurement of the theoretically predicted second-order Faraday coefficients, along with the chirality and Verdet constant of optically active substances.

The second-order Faraday coefficient β, theoretically predicted to be correlated to the natural optical activity of a substance, is expected to show stronger signature for substances with higher chirality. Glucose and its enantiomer Fructose molecules were selected to collect the strongest evidence of β because of their high specific optical rotations.

The results obtained from the oscillating polarization polarimeter as well as dual-reference lock-in polarimeter show a lack of evidence of a substance’s β. This is attributed mainly to three reasons: large Verdet constant of water, which masks the behavior of the chiral solute; the dynamic range and sensitivity of the lock-in detector, which restricts the overall signal amplification and small signal detection; available oscillating magnetic field amplitude which provides higher amplifications for the

effect of nonlinear Faraday coefficients, but which is increasingly difficult to obtain.

Different chemical and optical approaches were made to suppress the background caused by the large Verdet constant of water in our measurements. The best suppression of the Verdet constant dominated lock-in signal at ω_M by 3 orders of magnitude was achieved from a long TGG crystal positioned precisely along the axis of the sample containing solenoid.

Further improvements in the B_{amp}, Verdet constant reduction by the aforementioned TGG positioning, and signal conditioning is expected to improve the ability for detecting second-order Faraday effect. However, the hitherto non-detectable low values of β for strongly chiral compounds and the need for a larger **B**-field renders its determination impractical for pharmaceutical and astrobiological applications.

5.2 Rotating Polarization Scheme

Chiral signatures present in extra-terrestrial samples provide an excellent indicator for the presence of life. However, it is impractical to prepare optically clean samples without DLS, required for conventional polarimeters, in an extraterrestrial environment. Therefore, it is crucial to be able to make measurements on samples with significant DLS.

The rotating polarization polarimeter discussed herein is immune to large amounts of DLS because it measures the *phase* of the desired sinusoidal component of the detected intensity, which is not affected by a significant loss of *amplitude* due to DLS. The rotating polarization polarimeter is a true modulator-phase measurement technique. Consequentially, it provides a significant advantage over other polarimeters for the detection

of chirality in the presence of up to three orders of magnitude more depolarizing scattering.

The fact that we were able to use a life by-product, milk (which contains lactose, a chiral substance) as our scatterer and yet neglect its chirality in these measurements reflects the fact that the sensitivity of this current polarimeter setup is considerably less than that of a conventional polarimeter operating in the absence of DLS. Of course, this is an improper comparison, since detecting chirality in the presence of significant DLS is a very difficult problem, akin to the problem of imaging through turbid media, another unsolved optical problem. And it is much more difficult than detecting chirality in the absence of DLS. Indeed, for astrobiology, the latter problem is utterly irrelevant, while the problem of detecting chirality in the presence of significant DLS is crucial.

Upon improving the mechanical stability and electronics, the sensitivity of this polarimeter is expected to increase to that of conventional polarimeters in the absence of DLS. Improving this polarimeter design's robustness, compactness, weight, and energy-efficiency could eventually make it ideal for space missions.

5.3 Harmonic Generation Scheme

The SH obtained from different crystals (materials and sizes) has a higher degree of linear polarization as compared to that of the input laser pulses as expected (up to 3 orders of magnitude). The polarization purity of the SH obtained from an optimal crystal is expected to be better than the GL polarizers. The NLO crystals have been observed as excellent analyzers of polarized light, and are expected to provide even higher ER with a purer polarized light.

5.4 Future Directions

A sensitive NLO crystal based polarimeter can be designed with a set of optimal, good optical quality crystals for selected NLO processes. The following polarimeter scheme is thought to potentially provide further improvement in the ER.

The SHG – SFG (Type-I) scheme mentioned in chapter 4 (Fig. 4.4) is thought to be optimal in order to obtain a high ER, signal linearity and large signal strengths. This scheme offers the advantage of simplicity of setup through fewer elements and geometry. However, it is understood to suffer from two major disadvantages:

a) Temporal separation of the fundamental and SHG pulses due to group velocity mismatch (GVM), which would need compensation in order to achieve best conversion efficiencies.
b) Generation of unwanted 3H signal from both undesired nonlinear processes, and desired SFG process but with undesired components of the fundamental and the SH beam.

These disadvantages can be addressed by an improved design that utilizes separate paths for the fundamental and SH beams with pulse delays in both arms to improve the temporal overlap, and a noncollinear SFG process in the analyzer crystal that will produce the desired 3H output in a direction other than the pump and probe beams. The noncollinear geometry allows an added advantage of spatial filtering of the light produced as a result of any nonlinear processes from the fundamental and SH beams, as well as the beams themselves.

The 3H intensity derived through the noncollinear phasematched SFG process would be of the same order as the intensity obtained in the collinear scheme. The other advantages and disadvantages mentioned for the collinear scheme are retained in the noncollinear scheme.

Using a thicker SFG crystal would provide with further improvements. It improves the conversion efficiency of the phasematched SFG process, and simultaneously suppresses the conversion efficiency of non-phasematched processes by increasing the phase mismatch. Also, due to the sinc^2 dependence of the conversion efficiency on phase mismatch, 3H obtained from non-phasematched SFG processes exhibit different sinc^2 oscillations vs. wavelength than the phasematched SFG process (Fig. 5.1). The improved version of SHG - SFG (Type-I) noncollinear scheme is shown in Fig. 5.2.

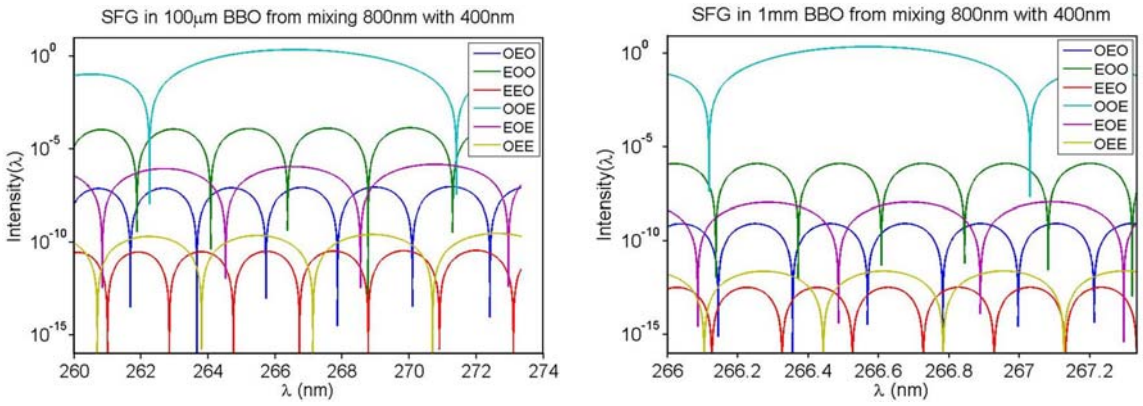

Figure 5.1: Simulated SFG spectrum for mixing 800nm with 400nm for different lengths of BBO.

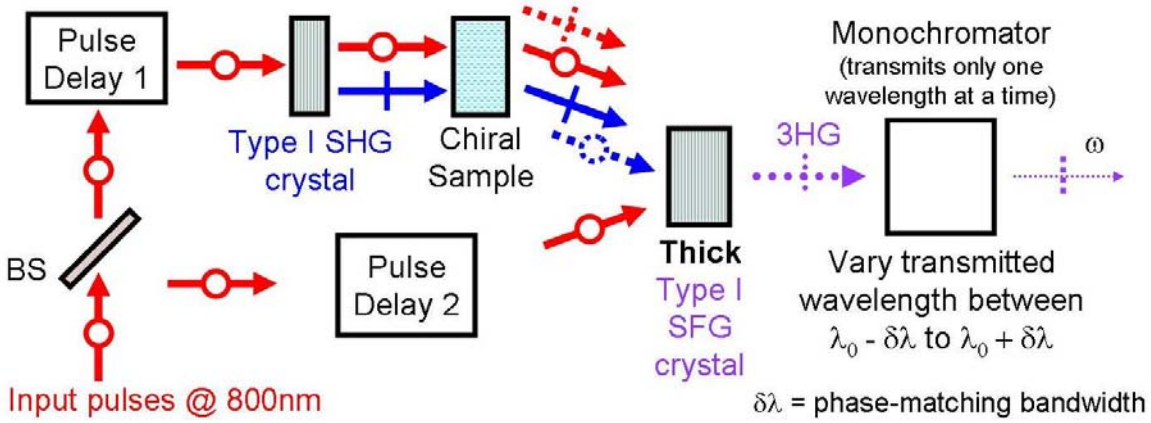

Figure 5.2: Proposed SHG – Noncollinear SFG (Type-I) scheme with thick SFG crystal and an oscillating monochromator.

A monochromator needs to be used then to separate the frequency components of 3H signal. Varying the transmitted wavelength between $\lambda_0 - \delta\lambda$ and $\lambda_0 + \delta\lambda$, where $\delta\lambda$ is the phase matching bandwidth, results in the 3H from the phasematched SFG process to go from a minimum through a maximum to a minimum. However, the 3H from non-phasematched SFG processes cross many more maxima and minima. Upon oscillating the transmitted wavelength from the monochromator between $\lambda_0 - \delta\lambda$ and $\lambda_0 + \delta\lambda$ at a frequency Ω, the 3H from the phasematched SFG process will oscillate at $2\,\Omega$ whereas the 3H from non-phasematched SFG processes will oscillate at higher harmonics of Ω. Therefore, a lock-in amplifier can be used to extract the phasematched signal to add extra sensitivity, and achieve further improvement in the ER.

Appendix A: Electronic Signal Processor

The electronic signal processor is based upon simple mathematical functions such as multiplication, phase-shifting, addition, subtraction to produce a real-time voltage signal at the sum and difference of desired harmonics of two reference frequencies ($p\omega_M \pm q\omega_L$, where p, q = 0,1,2…).

Let us start with the two reference voltage signals V_M and V_L, and also their π/2 phase-shifted waves.

$$V_M = V_{M0}\cos(\omega_M t + \phi_M) \qquad V_L = V_{L0}\cos(\omega_L t + \phi_L)$$

$$V_{M+\pi/2} = V_{M0}\cos(\omega_M t + \phi_M + \pi/2) \qquad V_{L+\pi/2} = V_{L0}\cos(\omega_L t + \phi_L + \pi/2)$$

To create a wave at frequency $\omega_M + \omega_L$, we perform the following:

$$V_M V_{L+\pi/2} + V_{M+\pi/2} V_L$$

$$= V_{M0}V_{L0}\left(\cos(\omega_M t + \phi_M)\cos(\omega_L t + \phi_L + \pi/2) + \cos(\omega_M t + \phi_M + \pi/2)\cos(\omega_L t + \phi_L)\right)$$

$$= V_{M0}V_{L0}\begin{pmatrix}\cos([\omega_M + \omega_L]t + [\phi_M + \phi_L] + \pi/2) + \cos([\omega_M - \omega_L]t + [\phi_M - \phi_L] - \pi/2) \\ +\cos([\omega_M + \omega_L]t + [\phi_M + \phi_L] + \pi/2) + \cos([\omega_M - \omega_L]t + [\phi_M - \phi_L] + \pi/2)\end{pmatrix}$$

$$= V_{M0}V_{L0}\begin{pmatrix}\cos([\omega_M + \omega_L]t + [\phi_M + \phi_L] + \pi/2) + \sin([\omega_M - \omega_L]t + [\phi_M - \phi_L]) \\ +\cos([\omega_M + \omega_L]t + [\phi_M + \phi_L] + \pi/2) - \sin([\omega_M - \omega_L]t + [\phi_M - \phi_L])\end{pmatrix}$$

$$= 2V_{M0}V_{L0}\cos([\omega_M + \omega_L]t + [\phi_M + \phi_L] + \pi/2)$$

To create a wave at frequency $\omega_M - \omega_L$, we perform the following:

$$V_M V_{L+\pi/2} - V_{M+\pi/2} V_L$$

$$= V_{M0} V_{L0} \left(\cos(\omega_M t + \phi_M) \cos(\omega_L t + \phi_L + \pi/2) - \cos(\omega_M t + \phi_M + \pi/2) \cos(\omega_L t + \phi_L) \right)$$

$$= V_{M0} V_{L0} \begin{pmatrix} \cos([\omega_M + \omega_L]t + [\phi_M + \phi_L] + \pi/2) + \cos([\omega_M - \omega_L]t + [\phi_M - \phi_L] - \pi/2) \\ -\cos([\omega_M + \omega_L]t + [\phi_M + \phi_L] + \pi/2) - \cos([\omega_M - \omega_L]t + [\phi_M - \phi_L] + \pi/2) \end{pmatrix}$$

$$= 2V_{M0} V_{L0} \cos([\omega_M - \omega_L]t + [\phi_M - \phi_L] - \pi/2)$$

Using the above mentioned tricks along with some electrical elements for dc-component rejection, phase-shifting, and amplification results into creation of a voltage signal at the desired mixed frequency (Fig. A.1-2).

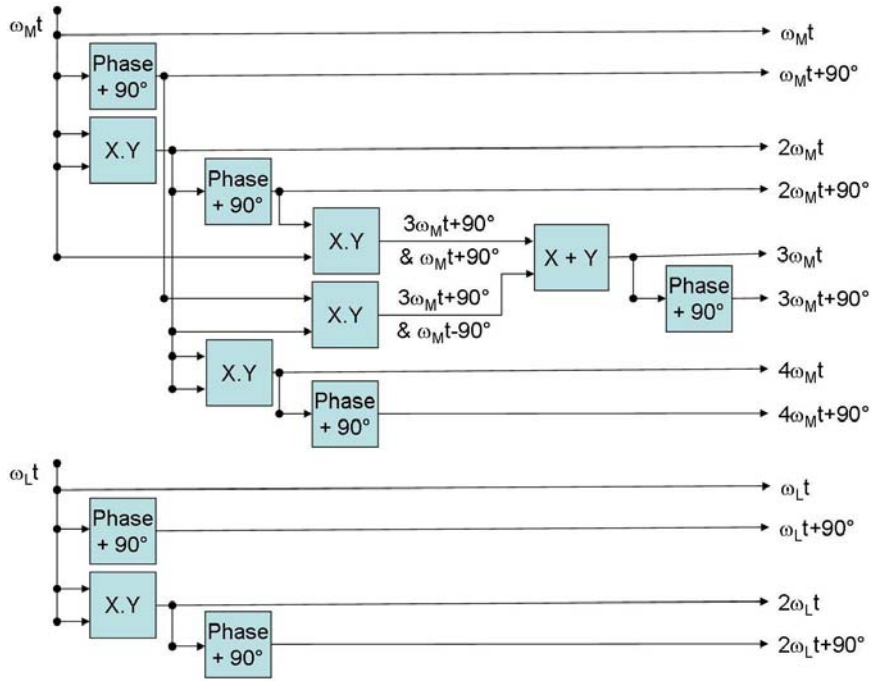

Figure A.1: Schematic for making harmonics and phase-shifts of ω_M and ω_L.

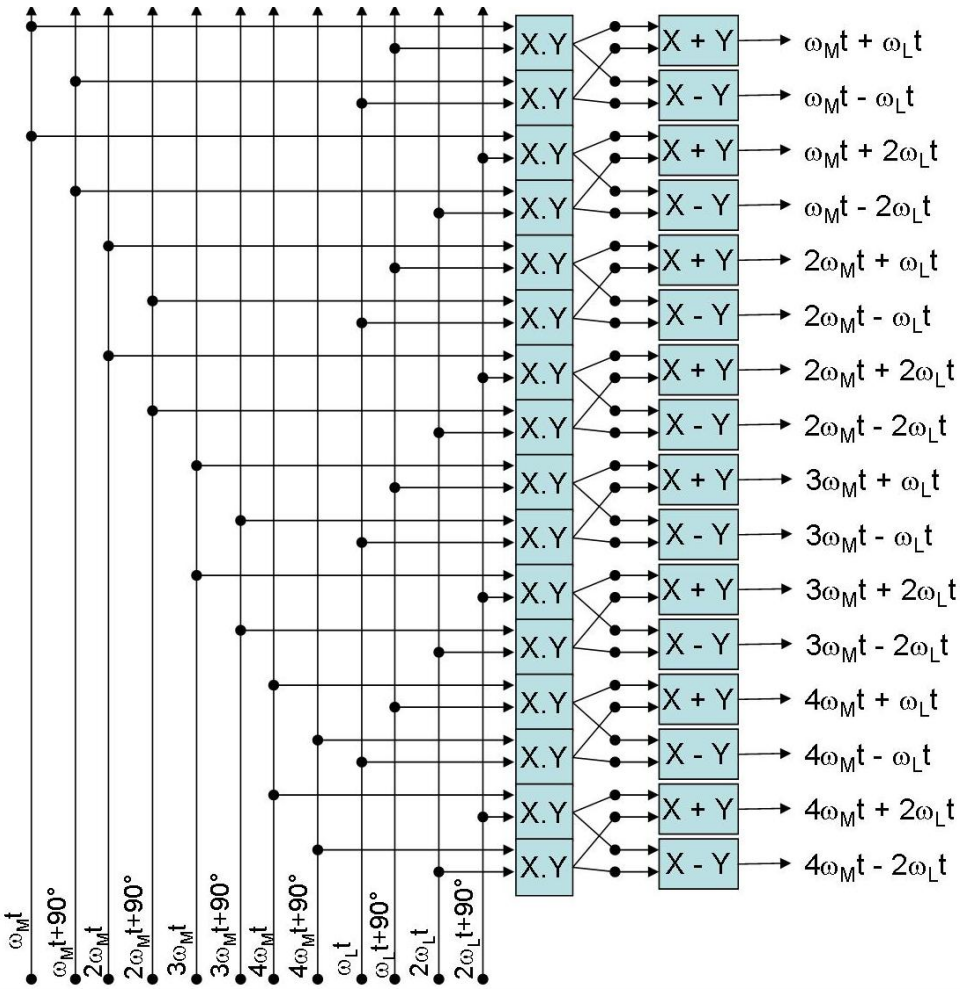

Figure A.2: Schematic for mixing the previously created harmonics of ω_M and ω_L to create a reference voltage signal at a combination frequency.

Appendix B: NLFE Model Calculations

Let us first calculate the output **E**-field for the setup shown in figure 2.1 using Jones calculus. The polarizer is oriented at θ_P with respect to horizontal, which sets the input **E**-field vector as

$$\vec{E}_{in} = E_0 \begin{bmatrix} \cos(\theta_P) \\ \sin(\theta_P) \end{bmatrix} \qquad [B.1]$$

The introduction of sample between the polarizer and analyzer then induces a rotation of polarization. The composite natural and induced rotation of polarization per unit path length produced by a medium under the influence of a magnetic field **B** is expressed as θ_S. The analyzer is set to pass vertically polarized component of the rotated signal field, and thus converting it into an intensity signal. The output **E**-field transmitted from the analyzer is given by

$$\vec{E}_{out} = \begin{bmatrix} 0 & 0 \\ 0 & 1 \end{bmatrix} \begin{bmatrix} \cos(\theta_S) & \sin(\theta_S) \\ -\sin(\theta_S) & \cos(\theta_S) \end{bmatrix} E_0 \begin{bmatrix} \cos(\theta_P) \\ \sin(\theta_P) \end{bmatrix} = \begin{pmatrix} 0 \\ E_0 \sin(\theta_S + \theta_P) \end{pmatrix}$$

$$\therefore \quad \vec{E}_{out} = E_{in} \sin(\theta_S + \theta_P)\hat{y} \qquad [B.2]$$

The ratio of intensity (or power) transmitted through the analyzer to input intensity (or power), which is proportional to the magnitude square of the output **E**-field, is expressed as

$$\frac{P_{out}}{P_{in}} = \frac{I_{out}}{I_{in}} = \frac{\left|\vec{E}_{out}\right|^2}{\left|\vec{E}_{in}\right|^2} = \frac{E_{in}^2 \sin^2(\theta_S + \theta_P)}{E_{in}^2} = \sin^2(\theta_S + \theta_P) \qquad [B.3]$$

$$\therefore\ P_{out} = P_{in}\sin^2\left(\theta_S + \theta_P\right) = P_{in}\sin^2\left(\Theta\right) \qquad [B.4]$$

where $\Theta = \theta_S + \theta_P$ is the angle (from horizontal) of instantaneous plane of polarization of the light incident upon the analyzer. Substituting for θ_S from eq. 2.3 while neglecting the contributions $O\left(B^3\right)$ to the polarization rotation, Θ becomes

$$\Theta = \theta_P + \alpha + \upsilon B + \beta B^2 \qquad [B.5]$$

where α (deg.m^{-1}) is the natural optical activity (chirality), υ (deg.T^{-1}m^{-1}) is the Verdet constant, and β (deg.T^{-2}m^{-1}) is the second order Faraday coefficient. The transmission-minimum position of the polarizer for a sample in absence of any **B**-field is used as the reference to calculate the leakage introduced for optical-heterodyning. $\theta_{LK}\left(=\theta_P+\alpha\right)$ is referred as leakage ($\theta_{LK} = 0$ when $\theta_P = -\alpha$). Then Θ reduces to

$$\Theta = \theta_{LK} + \upsilon B + \beta B^2 \qquad [B.6]$$

The solenoid is made to generate a sinusoidal magnetic field along the solenoid's axis.

$$B = B_{amp}\cos\left(\omega_M t\right) \qquad [B.7]$$

For small enough Θ, we can use the first-order small-angle approximation for sine, and express P_{out} as

$$P_{out} = P_{in}\ \Theta^2 \qquad [B.8]$$

Now we substitute Θ and **B** (eq. B.6, B.7) in eq. B.8 for P_{out} and it results into an expression with contributing terms showing signals at different harmonics of the **B**-field oscillation frequency ω, which is used as the reference frequency for lock-in detection.

$$P_{out} = P_{in}\left(\begin{array}{l}\theta_{LK}{}^2 + \left(\frac{1}{2}\upsilon^2 + \beta\theta_{LK}\right)B_{amp}{}^2 + \frac{3}{8}\beta^2 B_{amp}{}^4 \\ + \left(2\upsilon\theta_{LK}B_{amp} + \frac{3}{2}\upsilon\beta B_{amp}{}^3\right)\cos(\omega_M t) \\ + \left(\left(\frac{1}{2}\upsilon^2 + \beta\theta_{LK}\right)B_{amp}{}^2 + \frac{1}{2}\beta^2 B_{amp}{}^4\right)\cos(2\omega_M t) \\ + \frac{1}{2}\upsilon\beta B_{amp}{}^3\cos(3\omega_M t) + \frac{1}{8}\beta^2 B_{amp}{}^4\cos(4\omega_M t)\end{array}\right) \qquad [B.9]$$

The terms associated with the signal component at frequency ω_M show a linear dependence on the leakage θ_{LK}, with its slope exclusively proportional to υ. Similarly, the terms associated with the signal component at second-harmonic frequency $2\omega_M$ also show a linear dependence on the leakage θ_{LK}, however, its slope is exclusively proportional to β.

The dependence of P_{out} on leakage θ_{LK} is taken advantage of by oscillating the input polarization (amplitude θ_L, frequency $\omega_L\,(\sim \omega_M/10)$), thus splitting P_{out} components further into their sideband frequencies. This is experimentally achieved by introducing a TGG crystal Faraday rotator after the polarizer (Fig. 2.2). If θ_{FR} is the instantaneous rotation induced by the Faraday rotator, the output **E**-field becomes

$$\vec{E}_{out} = \begin{bmatrix} 0 & 0 \\ 0 & 1 \end{bmatrix} \begin{bmatrix} \cos(\theta_S) & \sin(\theta_S) \\ -\sin(\theta_S) & \cos(\theta_S) \end{bmatrix} \begin{bmatrix} \cos(\theta_{FR}) & \sin(\theta_{FR}) \\ -\sin(\theta_{FR}) & \cos(\theta_{FR}) \end{bmatrix} E_0 \begin{bmatrix} \cos(\theta_P) \\ \sin(\theta_P) \end{bmatrix}$$

$$\therefore \ \vec{E}_{out} = \begin{pmatrix} 0 \\ E_0 \sin(\theta_S + \theta_{FR} + \theta_P) \end{pmatrix} \quad \text{or} \quad \vec{E}_{out} = E_{in} \sin(\theta_S + \theta_{FR} + \theta_P)\,\hat{y} \qquad [B.10]$$

$$\frac{P_{out}}{P_{in}} = \frac{I_{out}}{I_{in}} = \frac{\left|\vec{E}_{out}\right|^2}{\left|\vec{E}_{in}\right|^2} = \frac{E_{in}^2 \sin^2(\theta_S + \theta_{FR} + \theta_P)}{E_{in}^2} = \sin^2(\theta_S + \theta_{FR} + \theta_P) \qquad [B.11]$$

$$\therefore \ P_{out} = P_{in} \sin^2(\theta_S + \theta_{FR} + \theta_P) = P_{in} \sin^2(\Theta) \qquad [B.12]$$

where $\Theta = \theta_S + \theta_{FR} + \theta_P$ is the angle (from horizontal) of instantaneous plane of polarization of the light incident upon the analyzer. Substituting for θ_S from eq. 2.3 while neglecting the contributions $O\left(B^3\right)$ to the polarization rotation, we get

$$\Theta = \theta_P + \theta_{FR} + \alpha + \upsilon B + \beta B^2 \qquad [B.13]$$

where $\theta_P + \theta_{FR} + \alpha$ act as leakage θ_{LK}. Ensuring $\theta_P = -\alpha$ by setting the position of the polarizer to transmission-minimum for a sample in absence of any **B**-field, and substituting for $\theta_{FR} = \theta_L \cos(\omega_L t)$ and B in Θ, it becomes

$$\Theta = \upsilon B_{amp} \cos(\omega_M t) + \beta {B_{amp}}^2 \cos^2(\omega_M t) + \theta_L \cos(\omega_L t) \qquad [B.14]$$

Using first-order small-angle sine approximation, P_{out} becomes

$$P_{out} = P_{in}\left(\begin{array}{l}
\frac{1}{2}\theta_L{}^2 + \frac{1}{2}\upsilon^2 B_{amp}{}^2 + \frac{3}{8}\beta^2 B_{amp}{}^4 \\
+\beta\,\theta_L B_{amp}{}^2 \cos(\omega_L t) + \frac{1}{2}\theta_L{}^2 \cos(2\omega_L t) \\
+\frac{3}{2}\upsilon\beta B_{amp}{}^3 \cos(\omega_M t) \\
+\upsilon\,\theta_L B_{amp}\left(\cos\left((\omega_M + \omega_L)t\right) + \cos\left((\omega_M - \omega_L)t\right)\right) \\
+\left(\frac{1}{2}\upsilon^2 B_{amp}{}^2 + \frac{1}{2}\beta^2 B_{amp}{}^4\right)\cos(2\omega_M t) \\
+\frac{1}{2}\beta\,\theta_L B_{amp}{}^2\left(\cos\left((2\omega_M + \omega_L)t\right) + \cos\left((2\omega_M - \omega_L)t\right)\right) \\
+\frac{1}{2}\upsilon\beta B_{amp}{}^3 \cos(3\omega_M t) + \frac{1}{8}\beta^2 B_{amp}{}^4 \cos(4\omega_M t)
\end{array}\right) \qquad \text{[B.15]}$$

The expression for P_{out} in eq. B.15 shows the leakage dependent terms seen earlier in eq. B.9 for each different harmonic of ω_M to appear at sideband frequencies around them. Also, note that the output power at sideband frequencies is symmetric.

The use of small-angle sine approximation to the second-order provides for a more accurate model for P_{out} when Θ is larger. However, this results in an explosion in the total number of terms in the expression for P_{out}.

$$P_{out} = P_{in}\left(\Theta^2 - \frac{1}{3}\Theta^4\right) \qquad \text{[B.16]}$$

P_{out} is calculated below for the beginning setup (Fig. 2.1) without the TGG crystal Faraday rotator.

$$
P_{out} = P_{in}\left(\begin{array}{l}
\left(\theta_{LK}^{2} - \frac{1}{3}\theta_{LK}^{4} + \left(\frac{1}{2}\upsilon^{2} + \beta\theta_{LK} - \upsilon^{2}\theta_{LK}^{2} - \frac{2}{3}\beta\theta_{LK}^{3}\right)B_{amp}^{2}\right. \\
\quad + \left(\frac{3}{8}\beta^{2} - \frac{1}{8}\upsilon^{4} - \frac{3}{2}\upsilon^{2}\beta\theta_{LK} - \frac{3}{4}\beta^{2}\theta_{LK}^{2}\right)B_{amp}^{4} \\
\quad \left. - \left(\frac{5}{8}\upsilon^{2}\beta^{2} + \frac{5}{12}\beta^{3}\theta_{LK}\right)B_{amp}^{6} - \frac{35}{384}\beta^{4}B_{amp}^{8}\right) \\
+ \left(\begin{array}{l}\left(2\upsilon\theta_{LK} - \frac{4}{3}\upsilon\theta_{LK}^{3}\right)B_{amp} \\ + \left(\frac{3}{2}\upsilon\beta - \upsilon^{3}\theta_{LK} - 3\upsilon\beta\theta_{LK}^{2}\right)B_{amp}^{3} \\ - \left(\frac{5}{6}\upsilon^{3}\beta + \frac{5}{2}\upsilon\beta^{2}\theta_{LK}\right)B_{amp}^{5} - \frac{35}{48}\upsilon\beta^{3}B_{amp}^{7}\end{array}\right)\cos(\omega_{M}t) \\
+ \left(\begin{array}{l}\left(\frac{1}{2}\upsilon^{2} + \beta\theta_{LK} - \upsilon^{2}\theta_{LK}^{2} - \frac{2}{3}\beta\theta_{LK}^{3}\right)B_{amp}^{2} \\ + \left(\frac{1}{2}\beta^{2} - 2\upsilon^{2}\beta\theta_{LK} - \beta^{2}\theta_{LK}^{2} - \frac{1}{6}\upsilon^{4}\right)B_{amp}^{4} \\ - \left(\frac{15}{16}\upsilon^{2}\beta^{2} + \frac{5}{8}\beta^{3}\theta_{LK}\right)B_{amp}^{6} - \frac{7}{48}\beta^{4}B_{amp}^{8}\end{array}\right)\cos(2\omega_{M}t) \\
+ \left(\begin{array}{l}\left(\frac{1}{2}\upsilon\beta - \frac{1}{3}\upsilon^{3}\theta_{LK} - \upsilon\beta\theta_{LK}^{2}\right)B_{amp}^{3} \\ - \left(\frac{5}{12}\upsilon^{3}\beta + \frac{5}{4}\upsilon\beta^{2}\theta_{LK}\right)B_{amp}^{5} - \frac{7}{16}\upsilon\beta^{3}B_{amp}^{7}\end{array}\right)\cos(3\omega_{M}t) \\
+ \left(\begin{array}{l}\left(\frac{1}{8}\beta^{2} - \frac{1}{24}\upsilon^{4} - \frac{1}{2}\upsilon^{2}\beta\theta_{LK} - \frac{1}{4}\beta^{2}\theta_{LK}^{2}\right)B_{amp}^{4} \\ - \left(\frac{3}{8}\upsilon^{2}\beta^{2} + \frac{1}{4}\beta^{3}\theta_{LK}\right)B_{amp}^{6} - \frac{7}{96}\beta^{4}B_{amp}^{8}\end{array}\right)\cos(4\omega_{M}t) \\
+ \left(\left(\frac{1}{12}\upsilon^{3}\beta + \frac{1}{4}\upsilon\beta^{2}\theta_{LK}\right)B_{amp}^{5} + \frac{7}{48}\upsilon\beta^{3}B_{amp}^{7}\right)\cos(5\omega_{M}t) \\
+ \left(\left(\frac{1}{16}\upsilon^{2}\beta^{2} + \frac{1}{24}\beta^{3}\theta_{LK}\right)B_{amp}^{6} + \frac{1}{48}\beta^{4}B_{amp}^{8}\right)\cos(6\omega_{M}t) \\
\left. + \frac{1}{48}\upsilon\beta^{3}B_{amp}^{7}\cos(7\omega_{M}t) + \frac{1}{384}\beta^{4}B_{amp}^{8}\cos(8\omega_{M}t)\right)
\end{array}\right) \qquad [B.17]
$$

References

[1] E. J. Gilham, "A high-precision photoelectric polarimeter", *Journal of Scientific Instruments* **34**, pp. 435-439 (1957).

[2] A. F. Browne, T. R. Nelson, and R. B. Northrop, "Microdegree polarimetric measurement of glucose concentrations for biotechnology applications", (IEEE, Durham, NH, USA, 1997), pp. 9-10.

[3] C. Graham, and R. F. Raab, "A molecular theory of natural and magneto-optical rotation in gases", *Proc. Phys. Soc.* **90**, pp. 417-426 (1967).

[4] "Synthetic calcite crystals", *Metals and Materials* **6**, p. 56 (1972).

[5] J. J. Brissot, "Problems related to the growth of artificial calcite single crystals", (IPC Sci. Technol. Press, Geneva, Switzerland, 1973), pp. 127-132.

[6] S. Hirano,Hirano; Shinichi (Tokyo, JP); Seiko Instruments & Electronics Ltd. (Tokyo, JP), "Process for manufacturing calcium carbonate single crystal ", *U. S. P. a. T. Office*,Patent # **4685995**

[7] K. Yanagisawa, K. Ioku, and N. Yamasaki, "Solubility and crystal growth of calcite in organic salt solutions under hydrothermal conditions", *Journal of Materials Science Letters* **14**, pp. 256-257 (1995).

[8] M. Surma, "Experimental evidence of the B-2 and B-3 dependent circular birefringence of chiral molecules in high magnetic fields", *Mol Phys* **93**, pp. 271-278 (1998).

[9] M. Surma, "Correlation between quadratic magnetic field induced circular birefringence and the natural optical activity of chiral media", *Mol Phys* **96**, pp. 429-433 (1999).

[10] M. Surma, "Magneto-optical circular birefringence of a chiral medium in high magnetic field", *Mol Phys* **90**, pp. 993-997 (1997).

[11] R. Zawodny, S. Wozniak, and G. Wagniere, "On quadratic dc magnetic field-induced circular birefringence and dichroism in isotropic chiral media", *Mol Phys* **91**, pp. 165-172 (1997).

[12] E. Munin, V. Romeu, C. Longo, A. B. Villaverde, and M. T. T. Pacheco, "Analysis of the picosecond magneto-optical phenomena in scattering media of biological interest", *Physics in Medicine and Biology* **47**, pp. 1519-1534 (2002).

[13] T. L. Thaler, P. R. Gibbs, R. P. Trebino, and A. S. Bommarius, "Search for Extraterrestrial Life Using Chiral Molecules: Mandelate Racemase as a Test Case", *Astrobiology* **6**, pp. 901-910 (2006).

[14] A. J. MacDermott, L. D. Barron, A. Brack, T. Buhse, A. F. Drake, R. Emery, G. Gottarelli, J. M. Greenberg, R. Haberle, R. A. Hegstrom, K. Hobbs, D. K. Kondepudi, C. McKay, S. Moorbath, F. Raulin, M. Sandford, D. W. Schwartzman, W. H. P. Thiemann, G. E. Tranter, and J. C. Zarnecki, "Homochirality as the signature of life: The SETH Cigar", *Planet Space Sci* **44**, pp. 1441-1446 (1996).

[15] C. Chou, H.-M. Tsai, K.-Y. Liao, L.-D. Chou, and P.-H. Huang, "Optical activity measurement by use of a balanced detector optical heterodyne interferometer", *Appl Optics* **45**, pp. 3733-3739 (2006).

[16] G. P. Temporao, and J. P. Von der Weid, "A Simple Low-Cost Broadband Fiber Optical Polarimeter", (Institute of Electrical and Electronics Engineers Inc., Piscataway, NJ 08855-1331, United States, Foz do Iguacu, Brazil, 2003), pp. 627-631.

[17] K. Hirabayashi, and C. Amano, "A Compact In-Line Polarimeter Using a Faraday Rotator", *IEEE Photonics Technology Letters* **15**, pp. 1740-1742 (2003).

[18] P. S. Westbrook, T. A. Strasser, and T. Erdogan, "In-Line Polarimeter Using Blazed Fiber Gratings", *IEEE Photonics Technology Letters* **12**, pp. 1352-1354 (2000).

[19] S. M. F. Nee, and T. Cole, "Effects of depolarization of polarimetric components on null ellipsometry", *Thin Solid Films* **313**, pp. 90-96 (1998).

[20] L. I. Chaikovskaya, and E. P. Zege, "Signal depolarization in the problems of laser sounding of scattering media with regard to multiple scattering", (Allerton Press, Preila, Lithuania, 1999), pp. 340-345.

[21] P. W. Atkins, and L. D. Barron, "Forward scattering of a beam of photons", *Molecular Physics* **18**, pp. 729-736 (1970).

[22] F. C. Mackintosh, J. X. Zhu, D. J. Pine, and D. A. Weitz, "Polarization memory of multiply scattered light", *Physical Review B (Condensed Matter)* **40**, pp. 9342-9345 (1989).

[23] A. P. Toropainen, "New method for measuring properties of nonhomogeneous materials by a two-polarization forward-scattering measurement", *IEEE Transactions on Microwave Theory and Techniques* **41**, pp. 2081-2086 (1993).

[24] V. V. Marienko, and S. N. Savenkov, "Active Stokes-Polarimetry with Presence of Light Background", *Ukr Fiz Zh*+ **39**, pp. 204-206 (1994).

[25] S. Barry, C. Nieswand, S. L. Prunty, H. M. Mansfield, and P. OLeary, "Bench test results on a new technique for far-infrared polarimetry", *Rev Sci Instrum* **68**, pp. 2037-2039 (1997).

[26] F. Delplancke, J. Badoz, and A. C. Boccara, "Multiple scattering in chiral media: border effects, reduced depolarization, and sensitivity limit", (SPIE-Int. Soc. Opt. Eng, San Diego, CA, USA, 1997), pp. 465-475.

[27] I. A. Vitkin, and E. Hoskinson, "Polarization studies in multiply scattering chiral media", *Opt Eng* **39**, pp. 353-362 (2000).

[28] L. I. Chaikovskaya, "Polarization estimation in the propagation of a narrow polarized beam through a multiply scattering medium", (SPIE-Int. Soc. Opt. Eng, Irkutsk, Russia, 2002), pp. 248-256.

[29] G. L. Cote, "Noninvasive optical glucose sensing-an overview", *Journal of Clinical Engineering* **22**, pp. 253-259 (1997).

[30] B. D. Cameron, and G. L. Cote, "Noninvasive glucose sensing utilizing a digital closed-loop polarimetric approach", *Ieee T Bio-Med Eng* **44**, pp. 1221-1227 (1997).

[31] G. L. Cote, and B. D. Cameron, "Noninvasive polarimetric measurement of glucose in cell culture media", *Journal of Biomedical Optics* **2**, pp. 275-281 (1997).

[32] B. D. Cameron, J. S. Baba, and G. L. Cote, "Optical polarimetry applied to the development of a noninvasive in vivo glucose monitor", (SPIE-Int. Soc. Opt. Eng, San Jose, CA, USA, 2000), pp. 66-77.

[33] M. J. McShane, R. J. Russell, M. V. Pishko, and G. L. Cote, "Glucose monitoring using implanted fluorescent microspheres", *IEEE Engineering in Medicine and Biology Magazine* **19**, pp. 36-45 (2000).

[34] J. S. Baba, and G. L. Cote, "Dual-detector polarimetry for compensation of motion artifact in a glucose sensing system", (SPIE-Int. Soc. Opt. Eng, San Jose, CA, USA, 2002), pp. 76-80.

[35] R. Tillman (Private communication, 2006).

[36] V. Kupershmidt,Sunshine Medical Instruments Inc. Sausalito, CA, "Pocket-type instrument for non-invasive measurement of blood glucose concentration", *U. S. P. a. T. Office*,Patent # **5398681**

[37] V. Kupershmidt,Sunshine Medical Instruments Inc. Sausalito, CA, "Method and apparatus for non-invasive phase sensitive measurement of blood glucose concentration", *U. S. P. a. T. Office*,Patent # **5448992**

[38] V. Kupershmidt, M. Kouchnir, and R. Petersen,Sunshine Medical Instruments Inc. Sausalito, CA, "Multiple wavelength polarization-modulated ellipsometer with phase-generated carrier", *U. S. P. a. T. Office*,Patent # **5548404**

[39] V. Kupershmidt,Sunshine Medical Instruments Inc. Sausalito, CA, "Optical phase modulator for high resolution phase measurements", *U. S. P. a. T. Office*,Patent # **5671301**

[40] E. Oliva, "Wedged double Wollaston, a device for single shot polarimetric measurements", *Astron Astrophys Sup* **123**, pp. 589-592 (1997).

[41] D. H. Goldstein, "Mueller Matrix Dual-Rotating Retarder Polarimeter", *Appl Optics* **31**, pp. 6676-6683 (1992).

[42] C. Chou, Y. C. Huang, C. M. Feng, and M. Chang, "Amplitude sensitive optical heterodyne and phase lock-in technique on small optical rotation angle detection of chiral liquid", *Jpn J Appl Phys 1* **36**, pp. 356-359 (1997).

[43] S. Y. Berezhna, I. V. Berezhnyy, and M. Takashi, "Dynamic photometric imaging polarizer-sample-analyzer polarimeter: instrument for mapping birefringence and optical rotation", *J Opt Soc Am A* **18**, pp. 666-672 (2001).

[44] S. L. Blakeney, S. E. Day, and J. N. Stewart, "Determination of unknown input polarisation using a twisted nematic liquid crystal display with fixed components", *Opt Commun* **214**, pp. 1-8 (2002).

[45] G. L. Cote, M. D. Fox, and R. B. Northrop, "Noninvasive Optical Polarimetric Glucose Sensing Using a True Phase Measurement Technique", *Ieee T Bio-Med Eng* **39**, pp. 752-756 (1992).

[46] K. Rochford, "Polarization and Polarimetry", in *Encyclopedia of Physical Science and Technology* (National Institute of Standards and Technology).

[47] M. K. Swami, S. Manhas, P. Buddhiwant, N. Ghosh, A. Uppal, and P. K. Gupta, "Polar decomposition of 3x3 Mueller matrix: a tool for quantitative tissue polarimetry", *Optics Express* **14**, pp. 9324-9337 (2006).

[48] D. Cote, and I. A. Vitkin, "Balanced detection for low-noise precision polarimetric measurements of optically active, multiply scattering tissue phantoms", *Journal of Biomedical Optics* **9**, pp. 213-220 (2004).

[49] S. Manhas, M. K. Swami, P. Buddhiwant, N. Ghosh, P. K. Gupta, and K. Singh, "Mueller matrix approach for determination of optical rotation in chiral turbid media in backscattering geometry", *Optics Express* **14**, pp. 190-202 (2006).

[50] E. S. Grin'ko, and Y. G. Shkuratov, "The scattering matrix of transparent particles of random shape in the geometrical optics approximation", *Optics and Spectroscopy* **93**, pp. 885-893 (2002).

[51] S. M. F. Nee, "Depolarization and principal Mueller matrix measured by null ellipsometry", *Appl Optics* **40**, pp. 4933-4939 (2001).

[52] D. W. Mueller, Jr., and A. L. Crosbie, "Analytical expressions for the radiation emergent from a scattering medium exposed to a polarized laser beam", *Journal of Quantitative Spectroscopy and Radiative Transfer* **67**, pp. 395-428 (2000).

[53] H. J. Schnorrenberg, M. Hengstebeck, and K. Schlinkmeier, "The attenuation of a coherent field by scattering", *Opt Commun* **117**, pp. 532-540 (1995).

[54] R. C. Chandan, "Dairy-based Ingredients", (Egan Press, 1997).

[55] V. S. Zapasskii, "Highly sensitive polarimetric techniques (review)", *Zhurnal Prikladnoi Spektroskopii* **37**, pp. 181-196 (1982).

[56] E. Hecht, "Optics", **3rd** edition (Addison-Wesley, Reading, Mass., 1998).

[57] "Polaroid Sheet Polarizers", (a webpage of CVI Lasers Inc.), http://www.cvilaser.com/Catalog/Pages/Template1.aspx?pcid=132, Accessed May, 2007.

[58] R. J. King, and S. P. Talim, "SOME ASPECTS OF POLARIZER PERFORMANCE", **4**, pp. 93-96 (1971).

[59] "Glan-Laser Polarizers", (a webpage of Karl Lambrecht Inc.), http://www.klccgo.com/glanlaser.htm, Accessed June, 2007.

[60] C. E. Moeller, and D. R. Grieser, "Observations of Defects in Crossed Glan-Thompson Polarizers", *Applied Optics* **8**, pp. 206-212 (1969).

[61] E. S. Yeung, L. E. Steenhoek, S. D. Woodruff, and J. C. Kuo, "Detector Based on Optical-Activity for High-Performance Liquid-Chromatographic Detection of Trace Organics", *Analytical Chemistry* **52**, pp. 1399-1402 (1980).

[62] N. Zheludev, S. Saltiel, and P. Yankov, "2nd-Harmonic Generators - a New Class of Light Polarizers and Analyzers", *Kvantovaya Elektronika* **14**, pp. 1495-1500 (1987).

[63] D. Y. Paraschuk, N. P. Zaitseva, and N. I. Zheludev, "Nonlinear frequency converters as sources and detectors of polarized light with linear polarization degree of 10/sup -9", *Proceedings of the SPIE - The International Society for Optical Engineering* **1841**, pp. 148-155 (1992).

[64] D. Y. Parashchuk, and A. S. Chirkin, "Precision laser light polarizers and analyzers based on nonlinear optical crystals", *Measurement Techniques Ussr* **38**, pp. 522-524 (1995).

[65] "BBO", (a webpage of Red Optronics), http://www.optical-components.com/BBO-crystal.html, Accessed May, 2007.

[66] R. W. Boyd, "Nonlinear optics", **2nd** edition (Academic Press, San Diego, Calif., 2003).

[67] Y. R. Shen, "The principles of nonlinear optics", (J. Wiley, New York, 1984).

[68] R. L. Sutherland, "Handbook of nonlinear optics", (Marcel Dekker, New York, 1996).

[69] S. M. Saltiel, P. D. Yankov, and N. I. Zheludev, "Second harmonic generation as a method for polarizing and analyzing laser light", *Applied Physics B (Photophysics and Laser Chemistry)* **B42**, pp. 115-119 (1987).

[70] G. G. Gurzadëiìan, V. G. Dmitriev, and D. N. Nikogosëiìan, "Handbook of nonlinear optical crystals", **3rd, rev.** edition (Springer, Berlin ; New York, 1999).

[71] R. Trebino, "Frequency-resolved optical gating : the measurement of ultrashort laser pulses", (Kluwer Academic, Boston, 2000).